Quantum scanning microscope for cold atoms

D. Yang, D. V. Vasilyev, C. Laflamme, M. A. Baranov, and P. Zoller
Center for Quantum Physics, Faculty of Mathematics, Computer Science and Physics, University of Innsbruck, 6020 Innsbruck, Austria and Institute for Quantum Optics and Quantum Information, Austrian Academy of Sciences, 6020 Innsbruck, Austria

(Received 23 May 2018; published 27 August 2018)

We present a detailed theoretical description of a recently proposed atomic scanning microscope in a cavity QED setup [D. Yang *et al.*, Phys. Rev. Lett. **120**, 133601 (2018)]. The microscope continuously observes atomic densities with optical subwavelength resolution in a nondestructive way. The superresolution is achieved by engineering an internal atomic dark state with a sharp spatial variation of population of a ground level dispersively coupled to the cavity field. Thus, the atomic position encoded in the internal state is revealed as a phase shift of the light reflected from the cavity in a homodyne experiment. Our theoretical description of the microscope operation is based on the stochastic master equation describing the conditional time evolution of the atomic system under continuous observation as a competition between dynamics induced by the Hamiltonian of the system, decoherence effects due to atomic spontaneous decay, and the measurement backaction. Within our approach we relate the observed homodyne current with a local atomic density and discuss the emergence of a quantum nondemolition measurement regime allowing continuous observation of spatial densities of quantum motional eigenstates without measurement backaction in a single experimental run.

DOI: 10.1103/PhysRevA.98.023852

I. INTRODUCTION

In recent work we proposed and discussed a scanning quantum microscope for cold atoms to continuously monitor atomic quantum dynamics [1]. The unique feature of our setup is that it acts a continuous measurement quantum device which, depending on the mode of operation, implements an emergent quantum nondemolition (QND) measurement of local density of an atomic quantum state with subwavelength resolution. It is therefore conceptually different from the familiar quantum gas microscope [2] that takes a fluorescence image of an instantaneous distribution of atoms over lattice sites in a many-body system placed in an optical lattice. In the present experiments, the quantum gas microscope operates as a destructive measurement device, making continuous observation of the atomic dynamics impossible. In contrast, our proposed microscope does not take pixelized images of atomic lattices at a given time, but scans in time the atomic quantum state on the subwavelength scale. In the movie mode, for a fixed focal region the microscope continuously records the atomic wave-packet dynamics. In the scanning mode with a good cavity, the microscope appears as a quantum nondemolition device such that a single spatial scan of the microscope focal region maps out the spatial density of an atomic motional eigenstate.

The quantum scanning microscope [1] continuously measures the atomic density within its focal region of subwavelength size via dispersive coupling of atoms to a laser-driven cavity, while the light reflected from the cavity is monitored by homodyne detection within the framework of weak continuous measurements [3–5]. It builds on the idea of using the atom-cavity coupling for measurement and control of atomic quantum systems, which was employed in experiments [6,7] as well as in theoretical proposals [8–13]. The microscope achieves the spatial superresolution by entangling the internal state of an atom with its position via engineering a spatially dependent dark state [14,15] (see Refs. [16,17] for pioneering experiments), however optimized such that the perturbation of the atomic system by the probe is negligible. This is in contrast to the existing methods for achieving subwavelength resolution by correlating the position of an atom with its internal state via either spatial potential gradients [18,19] or nonlinear optical response [14,15,20], which typically suffer from the presence of strong forces acting on atoms. We also note that, according to Ref. [21], advanced data processing makes it possible to reach a resolution comparable to the size of vibrational ground state of atoms in optical lattice wells, but still does not allow one to "look into" the lattice site and to monitor dynamics continuously.

It is the purpose of the present paper to elaborate on the detailed theory behind the operation of the quantum scanning microscope for cold atoms beyond the short presentation in Ref. [1], with emphasis on decoherence effects caused by atomic spontaneous emission and addressing experimental feasibility of the scheme. This also includes a thorough analysis of the effects of measurement backaction, the emergent quantum nondemolition regime, and the microscope resolution limit. The paper is organized as follows. In Sec. II we discuss the cavity QED (CQED) setup and operation principles of the microscope. The stochastic master equation (SME) describing the microscope operation will be derived in Sec. III starting from a quantum optical model for a CQED setup including the atomic spontaneous emission. Based on this derivation, in Sec. IV we present a detailed analysis of the movie and the scanning operation modes of the microscope illustrated by several (physically interesting) examples. We discuss the experimental feasibility of the proposed setup in Sec. V and summarize in Sec. VI.

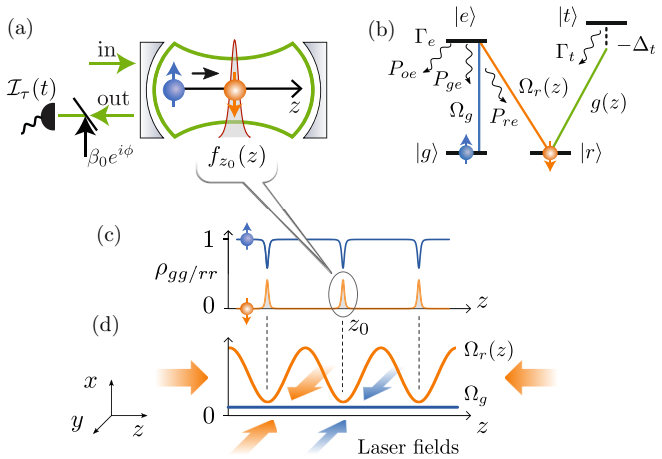

FIG. 1. Overview of the proposed quantum scanning microscope. (a) The appearance of an atom in the focal region of the microscope, as defined by the focus function $f_{z_0}(z)$, is accompanied by an internal spin flip, which shifts the resonance of a cavity mode and can be detected via homodyne detection. (b) Atomic level structure used to realize the microscope. The Λ system $|g\rangle, |e\rangle, |r\rangle$ supports a dark state $|D(z)\rangle$, of which the spin structure is correlated with the position of the atom due to the spatially varying Rabi frequency $\Omega_r(z)$. This internal spin is detected via dispersively coupling the $|r\rangle \to |t\rangle$ transition to a cavity mode. Atomic spontaneous emission, as shown by the wavy lines, results in imperfections in the microscope performance. Here $\Gamma_{e(t)}$ is the spontaneous-emission rate for the level $|e\rangle$ ($|t\rangle$) and P_{je} (with $j = g, r, o$) denotes the branching ratio for the emission channel $|e\rangle \to |j\rangle$, with $|o\rangle$ denoting atomic levels outside the four-level system under consideration. (c) Subwavelength spin structure of the atomic dark state $|D(z)\rangle$ and (d) corresponding laser configuration (see the description in Secs. II and III D).

II. MICROSCOPE SETUP AND OPERATION PRINCIPLES

We find it worthwhile to start our discussion with a summary of the microscope operation principles, before entering technical details. In the present paper we will focus on single-particle experiments illustrating the main concepts, which, however, are immediately applicable to many-body systems [1]. The basic idea behind the quantum scanning microscope is to entangle, with subwavelength resolution, the position of an atom with its internal state such that the observation of the internal state provides information about the atomic position. In the proposed setup (cf. Fig. 1 and [1]), the entanglement is achieved by using a position-dependent dark state in an atomic Λ system, which realizes an internal state flip in a region of an optical subwavelength size (the focal region of the microscope) [14–17,22,23]. Via a dispersive coupling of one of the internal atomic states to a cavity mode, the change in the internal state of an atom entering the focal region is detected nondestructively as a shift in the mode resonance frequency, which is revealed as a phase shift of the laser light reflected from the cavity in a homodyne measurement.

To be more specific, we consider an atom (or system of atoms) with two internal ground (spin) states $|g\rangle$ and $|r\rangle$ and one excited state $|e\rangle$ moving along the z axis (see Fig. 1) and we assume strong confinement in the other directions. The Hamiltonian describing a one-dimensional (1D) atomic motion is

$$\hat{H}_{A,E} = \frac{\hat{p}_z^2}{2m} + V(\hat{z}), \tag{1}$$

where $V(\hat{z})$ is an external (off-resonant) optical potential constraining the motion alone the z axis, which we assume to be identical for all atomic internal states. To entangle the position of an atom with its internal state, we form a Λ system with two Rabi frequencies: a constant weak Ω_g and a strong position-dependent (periodic) $\Omega_r(z)$ indicated in Figs. 1(b) and 1(d) by the blue and orange, respectively. Note that, in contrast to Refs. [22,23], here the Rabi frequency $\Omega_r(z)$ is never zero, $\Omega_r(z) > 0$. This configuration, as explained in detail in Sec. III D, makes it possible to create a dark state

$$|D(z)\rangle \sim \Omega_r(z)\,|g\rangle - \Omega_g\,|r\rangle\,, \tag{2}$$

with a subwavelength spatial structure without generating a noticeable nonadiabatic potential barrier, thus minimizing backaction. In the dark state [see Fig. 1(c)], the internal state $|r\rangle$ is partially populated only in the narrow focal regions of size $\sigma \ll \lambda_0$ near the minima of $\Omega_r(z)$, which creates the desired internal-state–position entanglement.

To detect an atom in the internal state $|r\rangle$ and therefore inside the focal region, we place the atomic system into a laser-driven optical cavity [see Fig. 1(a)] such that the driven cavity mode [the green area in Fig. 1(a) and the green line in Fig. 1(b)] couples the state $|r\rangle$ to another excited atomic state $|t\rangle$ with detuning Δ_t and strength $g(z)$ (the z dependence is due to a spatial profile of the cavity mode). For a large detuning $|\Delta_t| \gg |g(z)|$, this coupling generates a local dispersive interaction between the atom and the cavity mode. As detailed in Sec. III C, this interaction can be written as

$$\hat{H}_{\rm coup} = \mathcal{A} f_{z_0}(\hat{z})\,\hat{c}^\dagger \hat{c}, \tag{3}$$

where $\hat{c}^\dagger(\hat{c})$ is the photon creation (annihilation) operator for the cavity mode and

$$\mathcal{A} f_{z_0}(\hat{z}) = \frac{\hbar g^2(\hat{z})}{\Delta_t} |\langle r|D(z)\rangle|^2 = \frac{\hbar g^2(\hat{z})}{\Delta_t}\rho_{rr} \tag{4}$$

defines a sharply peaked focusing function $f_{z_0}(\hat{z})$ of resolution (width) σ around the focal point z_0 [the minimum of $\Omega_r(z)$] [see Figs. 1(c) and 1(d)]. Here $\mathcal{A}$ is the coupling strength with the dimension of energy, chosen in such a way that the matrix element of the focusing function over the atomic motional eigenstates are of order 1 (the precise definition will be given below in Sec. III, together with discussion of the effects related to a finite lifetime of the levels $|t\rangle$ and $|e\rangle$).

The dispersive coupling (3) implies that the presence of an atom inside the focal region defined by $f_{z_0}(z)$ shifts the cavity resonance, which can be detected via homodyne measurement. In such a measurement the output field of the cavity is combined with a local oscillator with phase ϕ, resulting in a homodyne current of the form (see Sec. III)

$$I(t) = \sqrt{\kappa}\langle \hat{X}_\phi \rangle_c + \xi(t). \tag{5}$$

Here $\hat{X}_\phi \equiv e^{i\phi}\hat{c}^\dagger + e^{-i\phi}\hat{c}$ is the associated quadrature operator of the cavity mode, κ is the cavity damping rate, $\xi(t)$ is the shot noise of the electromagnetic field, and $\langle \cdots \rangle_c \equiv {\rm Tr}\{\cdots \rho_c(t)\}$ refers to an expectation value with respect to the density

matrix of the joint atom-cavity system, conditioned on the measurement outcome. The evolution of $\rho_c(t)$ is governed by a SME to be derived in Sec. III. Based on this equation, we present a detailed discussion of the two operation modes of the microscope, the movie mode (Sec. IV A) and the scanning mode (Sec. IV B), and establish in both cases the connection between the measured homodyne current and the atomic motional quantum state.

In the movie mode, the microscope is focused at a given (fixed) position z_0 to "record a movie" of an atomic wave packet passing through the observation region, which in the example discussed below will be illustrated by a coherent state in a harmonic potential $V(z)$. This requires the cavity response time $\tau_C = 1/\kappa$ being much smaller than the typical timescale $1/\omega$ associated with the atomic motion, where ω is an oscillation frequency, i.e., we are in the bad cavity limit $\kappa \gg \omega$. In this case, as shown in Sec. IV A, the homodyne current follows the expectation value of the focusing function $\langle f_{z_0}(\hat{z})\rangle_c = \mathrm{Tr}\{f_{z_0}(\hat{z})\tilde{\rho}_c(t)\}$ instantaneously with $\tilde{\rho}_c(t)$ the atomic conditional density matrix,

$$I(t) = 2\sqrt{\gamma}\langle f_{z_0}(\hat{z})\rangle_c + \xi(t). \tag{6}$$

Here $\gamma = (4\mathcal{A}\mathcal{E}/\hbar\kappa)^2$ is the effective coupling rate for the measurement with $\mathcal{E}$ the amplitude of the driving laser field. Therefore, the measured homodyne current $I(t)$ in this mode directly probes the time evolution of the local atomic density at z_0 with spatial resolution σ. We note that the measurement backaction is proportional to γ (detailed in Sec. IV A), while the signal strength is to proportional to $\sqrt{\gamma}$ [see Eq. (6)]. As a consequence, we can minimize the backaction by taking small γ and obtain a good signal-to-noise ratio (SNR) by averaging over repeated runs of the experiment.

In the scanning mode we consider the good cavity limit $\kappa \ll \omega$ and perform a slow scan of the focal point $z_0 \equiv z_0(t)$ across a spatial region of interest. In this case, the cavity operates effectively as a low-pass filter for both the measured photocurrent and the vacuum fluctuations of the electromagnetic field perturbing the atomic system under observation. As a result (see Sec. IV B), the homodyne current traces the atomic dynamics at z_0 averaged over many oscillation periods such that the current is related only to the diagonal part $\hat{f}^{(0)}_{z_0} = \sum_n |n\rangle\langle n|f_{z_0}(\hat{z})|n\rangle\langle n|$ of the focusing function in the basis of the eigenstates $|n\rangle$ of the motional Hamiltonian $\hat{H}_{A,E}$ [Eq. (1)]. The vacuum fluctuations also couple mainly to $\hat{f}^{(0)}_{z_0}$ and hence do not interfere with the measurement, thus leading to a high SNR. The overall effect can be described as emergence of a new observable $\hat{f}^{(0)}_{z_0}$ which commutes with $\hat{H}_{A,E}$ and therefore represents a QND observable allowing for continuous quantum measurement without backaction [24–28]. Thus the microscope in the scanning mode appears as an effective QND device. Below we show (see Sec. IV B) that a single scan of the microscope with spatial subwavelength resolution σ will initially collapse (on a fast timescale $\sim 1/\gamma$) the atomic state to one of the motional eigenstates $|n\rangle$. The following (slow) spatial scan will map out the spatial density of $|n\rangle$. The scan of this spatial density will be reflected in the homodyne current

$$I(t) = 2\sqrt{\gamma}\langle n|\hat{f}^{(0)}_{z_0(t)}|n\rangle + \xi(t). \tag{7}$$

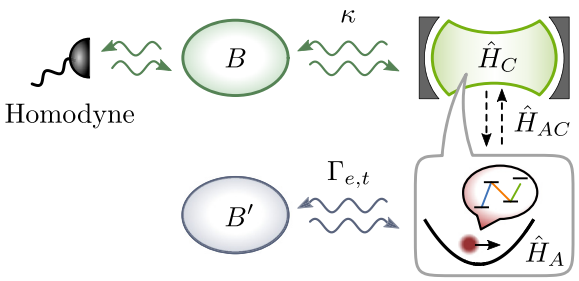

FIG. 2. Schematics of the quantum optical model for the microscope. It consists of the atomic system which we would like to measure (described by the Hamiltonian $\hat{H}_A$), the cavity mode which enables the measurement (described by the Hamiltonian $\hat{H}_C$ and coupled to the atom via the Hamiltonian $\hat{H}_{AC}$), and external baths (B and B'). Bath B is a 1D electromagnetic field (optical fiber), which couples to the cavity mode and is under continuous homodyne detection. Bath B' is a 3D electromagnetic field, which couples to the atom and gives rise to the atomic spontaneous emission.

We wish to elaborate briefly on the physics of the emergent QND measurement. We first note that the spatially localized focusing function $f_{z_0}(\hat{z})$ does *not* commute with the atomic motional Hamiltonian $\hat{H}_{A,E}$ and therefore is not an *a priori* QND observable. In the good cavity regime, however, the homodyne current probes only the diagonal part $\hat{f}^{(0)}_{z_0}$ of $f_{z_0}(\hat{z})$, which becomes the emergent QND observable. In fact, this is valid for an arbitrary observable (see Ref. [1]) and was recently used in a proposal for measuring the number of atoms via a dispersive coupling to a good cavity [29].

While the discussion in the present paper will focus on the theory of the quantum scanning microscope for (motion of) single particles, these concepts generalize to many-body quantum systems. This was illustrated in [1] (see also Ref. [11] therein) with the example of Friedel oscillations caused by an impurity in a Fermi gas.

III. QUANTUM OPTICAL MODEL

In this section we describe the quantum optical model for the scanning microscope of Sec. II. We will formulate our model in the language of a quantum stochastic Schrödinger equation (QSSE) (see, e.g., Chap. 9 in Ref. [5] for an introduction), which describes the evolution of the joint atom-cavity system interacting with an external electromagnetic field environment (Sec. III A). In Sec. III B we take this QSSE as the starting point to derive the SME for continuous homodyne detection of the cavity output field (see, e.g., Chap. 20 in Ref. [5] for an introduction). By further eliminating the atomic internal degrees of freedom (DOFs), we arrive in Sec. III C at a SME describing the dynamics of the microscope. Furthermore, we discuss the engineering of the subwavelength focusing function and the signal filtering for homodyne detection in Secs. III D and III E, respectively.

A. Quantum stochastic Schrödinger equation

We consider the quantum optical model of the quantum scanning microscope as shown schematically in Fig. 2. The time evolution of the total system is described by the (Itô)

QSSE [4,5] for the atom-cavity system and the external electromagnetic field (bath DOFs),

$$d|\Psi\rangle = -\left[\frac{i}{\hbar}\hat{H}_S + \frac{\kappa}{2}\hat{c}^\dagger\hat{c} + \frac{1}{2}(\Gamma_t\hat{\sigma}_{tt} + \Gamma_e\hat{\sigma}_{ee})\right]|\Psi\rangle\, dt + \sqrt{\kappa}\hat{c}\, d\hat{B}^\dagger(t)|\Psi\rangle + \sum_{\substack{n=e,t\\ j=g,r}}\int du\sqrt{\Gamma_n P_{jn}N_{jn}(u)}\hat{\sigma}_{jn} \times e^{-ik_0u\hat{z}}d\hat{B}^\dagger_{jn}(u,t)\,|\Psi\rangle\,. \quad (8)$$

Here the first line includes the coherent evolution under the atom-cavity Hamiltonian $\hat{H}_S$, the cavity damping, and the atomic decay, while the second and third lines represent the cavity-bath coupling and atomic spontaneous emission including recoil, respectively. Below we go through each term of Eq. (8) in detail.

We start with $\hat{H}_S$, which consists of three parts,

$$\hat{H}_S = \hat{H}_A + \hat{H}_{AC} + \hat{H}_C. \quad (9)$$

Here $\hat{H}_A = \hat{H}_{A,E} + \hat{H}_{A,I}$ is the atomic Hamiltonian, with $\hat{H}_{A,E}$ describing the external motion of the atom in one dimension [cf. Eq. (1)] and $\hat{H}_{A,I}$ representing the internal structure of the atom [see Fig. 1(b)], which in a rotating frame is given by

$$\hat{H}_{A,I} = -\hbar\Delta_t\hat{\sigma}_{tt} + \frac{\hbar}{2}[\Omega_g\hat{\sigma}_{ge} + \Omega_r(z)\hat{\sigma}_{re} + \text{H.c.}]. \quad (10)$$

Here we have adopted the notation $\hat{\sigma}_{ij} \equiv |i\rangle\langle j|$. For simplicity, we assume a resonant drive on both the $|g\rangle \to |e\rangle$ and $|r\rangle \to |e\rangle$ transitions and thus exact Raman resonance, while the transition $|r\rangle \to |t\rangle$ is coupled to the cavity mode with off-resonant detuning $\Delta_t = \omega_C - \omega_{tr}$, where ω_C is the frequency of the cavity mode. The coupling between the cavity mode and the atomic transition $|r\rangle \to |t\rangle$ is described by the Hamiltonian

$$\hat{H}_{AC} = \hbar g(\hat{z})(\hat{c}^\dagger\hat{\sigma}_{rt} + \text{H.c.}), \quad (11)$$

where $\hat{c}$ ($\hat{c}^\dagger$) is the destruction (creation) operator of the cavity mode and $g(z)$ is the coupling strength determined by the spatial profile of the cavity mode. The cavity mode is resonantly driven by a classical laser beam with amplitude $\mathcal{E}$ (assumed real for simplicity), as described by the Hamiltonian $\hat{H}_C$ in the rotating frame,

$$\hat{H}_C = i\hbar\sqrt{\kappa}\mathcal{E}(\hat{c} - \hat{c}^\dagger), \quad (12)$$

with κ the damping rate of the cavity mode.

The cavity is coupled to a waveguide (optical fiber) representing the input and output channels of our system. These external electromagnetic modes are modeled as a 1D bosonic bath (shown as bath B in Fig. 2) and quantum optics introduces corresponding bosonic noise operators $\hat{b}(t)$ and $\hat{b}^\dagger(t)$, satisfying white-noise commutation relations $[\hat{b}(t), \hat{b}^\dagger(t')] = \delta(t-t')$ [4,5]. In the Itô QSSE (8) these noise operators are transcribed as Wiener operator noise increments, $\hat{b}(t)dt \to d\hat{B}(t)$ and $\hat{b}^\dagger(t)dt \to d\hat{B}^\dagger(t)$. With the incident coherent field driving the cavity already transformed into the classical field in Eq. (12), we can assume vacuum inputs and thus have the Itô table [4,5]

$$d\hat{B}(t)d\hat{B}^\dagger(t) = dt,$$
$$d\hat{B}^\dagger(t)d\hat{B}(t) = d\hat{B}(t)d\hat{B}(t) = d\hat{B}^\dagger(t)d\hat{B}^\dagger(t) = 0. \quad (13)$$

In this formalism the cavity coupling to the waveguide is now described by the second line of Eq. (8).[1] Apart from such an explicit cavity-bath coupling term, the inclusion of the 1D bosonic bath also introduces a cavity damping term $-\kappa\hat{c}^\dagger\hat{c}/2$ in the first line of Eq. (8). Mathematically, this non-Hermitian term appears as an Itô correction, when transforming the Stratonovich QSSE to Itô form [4,5].

The third line of Eq. (8) represents spontaneous emission of the atom into the 3D background electromagnetic modes (shown as bath B' in Fig. 2), as familiar from the theory of laser cooling [5]. Here Γ_n (with $n = e, t$) is the spontaneous-emission rate of the excited states [see Fig. 1(b)] and P_{jn} (with $j = g, r$) denotes the branching ratio for the emission channel $|n\rangle \to |j\rangle$. The function $N_{jn}(u)$ reflects the dipole emission pattern of channel $|n\rangle \to |j\rangle$ which, for the 1D atomic motion considered here, depends on a single variable $u \equiv \cos\varphi \in [-1, 1]$, with φ the angle between the wave vector of the emitted photon and the z axis. The spontaneous emission is accompanied by the momentum recoil to the 1D atomic motion, which is accounted for by the operator $e^{ik_0u\hat{z}}$, with k_0 the wave vector of the emitted photons (for simplicity of notation assumed to be the same for all the emission channels). For each emission channel $|n\rangle \to |j\rangle$ and for each emission direction u, we introduce the corresponding quantum noise increment $d\hat{B}^\dagger_{jn}(u,t)$ to describe the relevant electromagnetic modes. Assuming a 3D bath initially in the vacuum state, they obey the Itô table [5]

$$d\hat{B}_{jn}(u,t)d\hat{B}^\dagger_{j'n'}(u',t) = dt\delta(u-u')\delta_{jj'}\delta_{nn'}, \quad (14)$$

with other entries in the Itô table equal to zero. Finally, the explicit atom-bath coupling term is necessarily accompanied by the corresponding Itô correction, given by the decay term $-(\Gamma_t\hat{\sigma}_{tt} + \Gamma_e\hat{\sigma}_{ee})/2$ in the first line of Eq. (8).

Having established the QSSE (8) as the basic dynamical equation for our model system, we will in the following section derive the SME for the atom-cavity system. This SME describes the evolution of the atom-cavity system under homodyne measurement of the cavity output, conditional to observing a particular homodyne current trajectory.

B. Stochastic master equation for homodyne measurement

Let us consider homodyne measurement of the output light of the cavity. In such a measurement, the output light from the cavity is mixed with a reference laser (a local oscillator), allowing the measurement of the quadrature $d\hat{Q}(t)$ of the 1D electromagnetic field bath [4,5]

$$d\hat{Q}(t) = d\hat{B}(t)e^{-i\phi} + d\hat{B}^\dagger(t)e^{i\phi}, \quad (15)$$

where ϕ is the phase of the local oscillator. The measurement will project the state of the bath onto an eigenstate of $d\hat{Q}(t)$

[1] The absence of the adjoint term is again due to our assumption $\sqrt{\kappa}\hat{c}^\dagger d\hat{B}(t)\,|\Psi\rangle = 0$ of vacuum inputs.

corresponding to the eigenvalue $dq(t)$, which defines the homodyne current via $dq(t) \equiv I(t)dt$. It can be shown [4,5] that the measurement outcome $dq(t)$ obeys a normal distribution centered at the mean value of the cavity quadrature, i.e.,

$$dq(t) \equiv I(t)dt = \sqrt{\kappa}\langle \hat{X}_\phi \rangle_c dt + dW(t), \tag{16}$$

where $\hat{X}_\phi = e^{i\phi}\hat{c}^\dagger + e^{-i\phi}\hat{c}$ as defined in Sec. II and $dW(t)$ is a random Wiener increment, which is related to the shot noise by $dW(t) = \xi(t)dt$. The expectation value $\langle \cdots \rangle_c = \mathrm{Tr}(\cdots \mu_c)$ is taken with a conditional density matrix μ_c of the joint atom-cavity system.

The evolution of μ_c is given by a SME derived from Eq. (8) by projecting out the bath DOFs following standard procedures [4,5],

$$\begin{aligned} d\mu_c = & -\frac{i}{\hbar}[\hat{H}_S, \mu_c]dt + \kappa \mathcal{D}[\hat{c}]\mu_c dt + \sqrt{\kappa}\mathcal{H}[\hat{c}e^{-i\phi}]\mu_c dW(t) \\ & + \Gamma_t \int du\, N_{rt}(u)\mathcal{D}[e^{-ik_0 u\hat{z}}\hat{\sigma}_{rt}]\mu_c dt \\ & - \frac{\Gamma_e P_{oe}}{2}\{\hat{\sigma}_{ee}, \mu_c\}dt \\ & + \Gamma_e \sum_{j=g,r} P_{je} \int du\, N_{je}(u)\mathcal{D}[e^{-ik_0 u\hat{z}}\hat{\sigma}_{je}]\mu_c\, dt. \end{aligned} \tag{17}$$

Here $\mathcal{D}[\hat{O}]\rho \equiv \hat{O}\rho\hat{O}^\dagger - \frac{1}{2}\hat{O}^\dagger\hat{O}\rho - \frac{1}{2}\rho\hat{O}^\dagger\hat{O}$ is the Lindblad superoperator and $\mathcal{H}[\hat{O}]\rho \equiv \hat{O}\rho - \mathrm{Tr}(\hat{O}\rho)\rho + \mathrm{H.c.}$ is a superoperator corresponding to homodyne measurement. As can be seen, the 1D electromagnetic field leads to both a decoherence term and a stochastic term [cf. the first line of Eq. (17)] to the system evolution, which represent the backaction of homodyne measurement. In contrast, spontaneous emission into the 3D electromagnetic field is not continuously monitored in our model setup and thus leads to pure decoherence, as captured by the last three lines of Eq. (17).

Incorporating the spontaneous-emission terms in Eq. (17) is important for a realistic description of an experiment. First, as is the case in most CQED experiments, we consider the levels $|r\rangle$ and $|t\rangle$ to form a closed cycling transition such that $|t\rangle \to |r\rangle$ is the only dipole-allowed spontaneous-emission channel for $|t\rangle$. Second, in contrast to $|t\rangle$, we allow $|e\rangle$ to have multiple spontaneous-decay channels. This includes decays to states $|g\rangle$ and $|r\rangle$, with branching ratios P_{ge} and P_{re}, respectively. In addition, $|e\rangle$ can also spontaneously decay outside the four-level system, which is modeled as a pure decay term in the third line of Eq. (17) with branching ratio $P_{oe} \equiv 1 - P_{ge} - P_{re}$.

To summarize, the SME (17) and the homodyne current (16) provide a complete description of the evolution of the joint atom-cavity system, subjected to continuous homodyne measurement of the cavity output in the presence atomic spontaneous emission. In Eqs. (16) and (17), the atomic DOFs include both the atom's external motion and its internal DOFs. In the next section we will further reduce our equations to a model where only the cavity mode and atomic external motion appear, while we adiabatically eliminate the atomic internal dynamics assuming the atomic system remains in a dark state [compare Eq. (2)].

C. Adiabatic elimination of the atomic internal dynamics

As mentioned in Sec. II, we are interested in a regime where (i) the external motion of the atom is much slower than its internal dynamics, $|\hat{H}_{A,E}| \ll |\hat{H}_{A,I}|$, and (ii) the atom is coupled to the cavity mode dispersively, $\Delta_t \gg g(z)$. In this regime, according to Eq. (17), we have a hierarchy of timescales, with the short timescale corresponding to the fast dynamics of the atomic internal DOFs and the much longer timescale corresponding to the slow dynamics of cavity mode plus the atomic external DOFs. This allows us to eliminate the atomic internal DOFs by an adiabatic assumption.

To be concrete, let us consider the eigenspectrum of $\hat{H}_{A,I}$ describing the atomic internal dynamics, which is shown in Fig. 11. As mentioned in Sec. II, it includes a dark state

$$|D(z)\rangle = \sin\alpha(z)|g\rangle - \cos\alpha(z)|r\rangle\,, \tag{18}$$

with the eigenenergy $E_D = 0$. This state is spectrally well separated from the other eigenstates, namely, the excited state $|t\rangle$, with the corresponding eigenenergy $E_t = -\hbar\Delta_t$; and the bright states

$$|\pm\rangle = \frac{1}{\sqrt{2}}[\pm|e\rangle + \cos\alpha(z)|g\rangle + \sin\alpha(z)|r\rangle], \tag{19}$$

with the corresponding energies $E_\pm(z) = \pm\hbar\Omega(z)/2$. Here we have defined the total Rabi frequency $\Omega(z) \equiv [\Omega_g^2 + \Omega_r^2(z)]^{1/2}$ and the mixing angle

$$\tan\alpha(z) = \Omega_r(z)/\Omega_g. \tag{20}$$

In the absence of $\hat{H}_{AC}$ or $\hat{H}_{A,E}$, the internal state of the atom will remain in the dark state $|D\rangle$. Thus, the joint atom-cavity system is described by a product state

$$\mu_c(t) = \rho_c(t) \otimes |D\rangle\langle D|\,, \tag{21}$$

where $\rho_c(t) \equiv \mathrm{Tr}_{A,I}[\mu_c(t)]$ is the reduced density matrix for the cavity mode and the atomic external motion, with $\mathrm{Tr}_{A,I}$ indicating a trace over the atomic internal DOFs.

Reintroducing $\hat{H}_{AC}$ and $\hat{H}_{A,E}$ couples the dark state $|D\rangle$ to the rest of the atomic internal states. The Hamiltonian $\hat{H}_{AC}$ couples $|D\rangle$ and $|t\rangle$ [see Eq. (11)]. The Hamiltonian $\hat{H}_{A,E}$ couples $|D\rangle$ and $|\pm\rangle$, due to the fact that the momentum operator $\hat{p}_z$ in $\hat{H}_{A,E}$ is nondiagonal in this position-dependent dark- and bright-state basis. Nevertheless, in the weak-coupling limit $|\hat{H}_{A,E}| \ll \hbar\Omega(z)$ and $|\hat{H}_{AC}| \ll \hbar|\Delta_t|$, the full density matrix $\rho_c(t)$ still preserves the separable form as in Eq. (21), except that for the atomic internal dynamics the dark state is weakly mixed with the excited states, which can be calculated in perturbation theory. The details of this derivation are presented in Appendix A. The resulting evolution of the reduced density matrix $\rho_c(t)$ reads

$$\begin{aligned} d\rho_c = & -\frac{i}{\hbar}[\hat{H}_{A,E} + \hat{H}_C + \hat{H}_{\mathrm{coup}} + V_{\mathrm{na}}(\hat{z}), \rho_c]dt \\ & + \kappa\mathcal{D}[\hat{c}]\rho_c dt + \sqrt{\kappa}\mathcal{H}[\hat{c}e^{-i\phi}]\rho_c dW(t) \\ & + \left(\frac{\Gamma_t}{\Delta_t^2}\mathcal{L}' + \mathcal{L}''\right)\rho_c dt. \end{aligned} \tag{22}$$

Correspondingly, the homodyne current is determined according to

$$dq(t) \equiv I(t)dt = \sqrt{\kappa}\mathrm{Tr}(\hat{X}_\phi\rho_c)dt + dW(t). \tag{23}$$

In Eq. (22), $\hat{H}_{\rm coup}$ describes the local dispersive coupling [cf. Eq. (3)] between the atom and the cavity mode,

$$\hat{H}_{\rm coup} = \frac{\hbar g^2(\hat{z})}{\Delta_t}[\cos\alpha(\hat{z})]^2\hat{c}^\dagger\hat{c} \equiv \mathcal{A} f_{z_0}(\hat{z})\hat{c}^\dagger\hat{c}, \tag{24}$$

and is parameterized in terms of a focusing function $f_{z_0}(\hat{z})$ [see Eq. (3)], which is a dimensionless and normalized function around z_0, and a coupling strength $\mathcal{A}$, with the dimension of energy. We choose the normalization $\int dz f_{z_0}(z) = \ell_0$, with ℓ_0 being the characteristic length scale of the system under measurement such that the matrix elements of $f_{z_0}(\hat{z})$ taken over the system states are of order 1. The spatial profile of $f_{z_0}(\hat{z})$ is inherited from the position dependence of the mixing angle $\alpha(z)$ and can be engineered easily by adjusting the Rabi frequencies Ω_g and $\Omega_r(z)$ of the Raman lasers. In Sec. III D we will discuss a laser configuration where $f_{z_0}(\hat{z})$ is peaked at z_0 with a nanoscale width.

Besides $\hat{H}_{\rm coup}$, Eq. (22) contains several additional terms, which do not contribute to the homodyne measurement and thus are imperfections for the evolution of the system. This includes first of all

$$V_{\rm na}(z) = \frac{\hbar^2}{2m}(\partial_z\alpha)^2 \tag{25}$$

as the lowest order nonadiabatic potential for the atomic external motion [22,23], originating from the spatially varying internal dark-state structure. As discussed in Sec. III D below, we can make this term small with a proper choice of the laser configuration.

Note also that in a driven optical cavity, the atom-cavity coupling $\hat{H}_{\rm coup}$ [Eq. (24)] gives rise to an optical lattice potential $V_{\rm OL}(\hat{z}) = \mathcal{A} f_{z_0}(\hat{z})\alpha_0^2$ for the atom, with $\alpha_0 = -2\mathcal{E}/\sqrt{\kappa}$ the amplitude of the stationary cavity field. This potential, however, can be straightforwardly compensated by introducing a small detuning $\Delta_r = g^2(z_0)\alpha_0^2/\Delta_t$ for the $|r\rangle \to |e\rangle$ transition, resulting in an optical potential $V_{\rm comp}(\hat{z}) = -\Delta_r[\cos\alpha(\hat{z})]^2$ for the atom, which compensates $V_{\rm OL}(\hat{z})$ in the spatial region of interest.

The Liouvillian $(\Gamma_t/\Delta_t^2)\mathcal{L}'$ in the last line of (22) describes the decoherence of the joint atom-cavity system, inherited from the atomic spontaneous emission in the channel $|t\rangle \to |r\rangle$, which is used to generate the dispersive atom-cavity coupling. The detailed expression of $\mathcal{L}'$ is given in Appendix A. Here we note that, although this decoherence term can be suppressed by increasing the detuning Δ_t, this will also reduce the dispersive coupling strength $\mathcal{A}$ [cf. Eq. (24)] and therefore the observed signal. As a consequence, $(\Gamma_t/\Delta_t^2)\mathcal{L}'$ serves as an intrinsic decoherence term for our dispersive atom-cavity coupling scheme and will have important impact on the performance of the microscope, to be discussed in Sec. IV.

Finally, $\mathcal{L}''$ in the last line of (22) describes decoherence due to the coupling between $|D\rangle$ and $|\pm\rangle$ resulting from the motion of the atom, the detailed expression of which is given in Appendix A. As shown there, $\mathcal{L}''$ can be made arbitrarily small by increasing the amplitude of Ω_g and $\Omega_r(z)$. We will neglect $\mathcal{L}''$ in the following.

To summarize, the SME (22) with internal states being eliminated and the corresponding expression for the homodyne current (23) constitute the basic dynamical equations governing the time evolution of the quantum scanning microscope and provide the basis of our discussion of the microscope operation in Sec. IV.

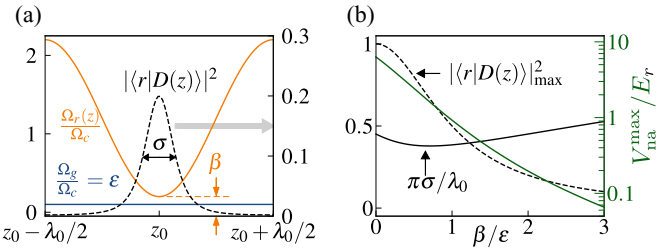

FIG. 3. Engineering the focusing function $f_{z_0}(z)$, which enables subwavelength detection of the atomic density via Eq. (3). (a) $f_{z_0}(z) \sim |\langle r|D(z)\rangle|^2$ (dashed line) is shown together with the Rabi frequencies for the internal Λ transition (see Fig. 1), $\Omega_r(z) = \Omega_c\{1 + \beta - \cos[k_0(z - z_0)]\}$ (light solid line) and $\Omega_g = \epsilon\Omega_c$ (dark solid line), for $\epsilon = \beta/2 = 0.1$. Adjusting β and ϵ enables adjusting the resolution σ (see the text). (b) Resolution σ, maximal overlap $|\langle r|D(z)\rangle|^2_{\max}$, and maximal value $V_{\rm na}^{\max}$ of the nonadiabatic potential $V_{\rm na}(z)$ (in units of the recoil energy E_r) as a function of β/ϵ, shown for $\epsilon = 0.1$. For $\beta/\epsilon \gtrsim 1$, $V_{\rm na}(z)$ is strongly suppressed.

D. Engineering the focusing function $f_{z_0}(\hat{z})$

By eliminating the internal DOFs of the atom, we arrive at a local dispersive coupling between the atom and the cavity mode [Eq. (24)], defined via the focusing function $f_{z_0}(\hat{z})$. We now show how to engineer the resolution of the focusing function down to the deep subwavelength regime and with negligible nonadiabatic potential.

Let us consider the two Raman laser beams being phase coherent, with the Rabi frequencies parametrized by

$$\Omega_g = \epsilon\Omega_c, \quad \Omega_r(z) = \Omega_c[1 + \beta - \cos k_0(z - z_0)], \tag{26}$$

where Ω_c is a large reference frequency (assumed real and positive for simplicity) and $0 < \epsilon \sim \beta \ll 1$. In practice, $\Omega_r(z)$ can be realized, e.g., by superimposing phase-coherent laser beams to form the standing wave $\Omega_c \cos k_0(z - z_0)$ along the z axis and another standing wave in an orthogonal direction, to provide the offset $\Omega_c(1 + \beta)$, as shown in Fig. 1(d).

The laser configuration (26) completely determines the focusing function [cf. Eqs. (20) and (24)], which is shown in Fig 3(a). We define the resolution σ of the focusing function as its full width at half maximum, which reads

$$\frac{\sigma}{\lambda_0} = \frac{\sqrt{2\beta}}{\pi}[\sqrt{2 + (\epsilon/\beta)^2} - 1]^{1/2}, \tag{27}$$

with $\lambda_0 = 2\pi/k_0$ the wavelength for the $|r\rangle \to |e\rangle$ transition. Thus, the resolution can be made subwavelength, by choosing $\epsilon \sim \beta \ll 1$.

Moreover, the laser configuration (26) allows for rendering the nonadiabatic potential $V_{\rm na}(z)$ negligible [cf. Eq. (25)]. In the regime of interest $\epsilon \sim \beta \ll 1$, such a nonadiabatic potential expanded around the focal point z_0 can be calculated with Eqs. (20) and (25) as

$$V_{\rm na}(z) = E_r\left\{\frac{4\epsilon k_0(z - z_0)}{\left[k_0^2(z - z_0)^2 + 2\beta\right]^2 + 4\epsilon^2}\right\}^2, \tag{28}$$

where $E_r = \hbar^2 k_0^2/2m$ is the recoil energy of the atom. As illustrated in Fig. 3(b), $V_{\rm na}(z)$ decreases rapidly with increasing the ratio β/ϵ. Physically, decreasing ϵ/β reduces the overlap between the dark state and the state $|r\rangle$, $|\langle r|D(z)\rangle|^2_{\rm max} = (1 + \beta^2/\epsilon^2)^{-1}$, such that the dark state varies more slowly in space, thus suppressing the corresponding nonadiabatic potential.

In fact, in the considered limit $\sigma \ll \lambda_0$, one can make both σ and $V_{\rm na}(z)$ arbitrarily small by choosing appropriate values of β and ϵ/β which scale as $\beta \sim (\sigma k_0)^2$ and $\epsilon/\beta \sim \sigma k_0 \sqrt{V_{\rm na}^{\rm max}/E_r}$, where $V_{\rm na}^{\rm max} = \max_z\{V_{\rm na}(z)\}$ is the maximal value of the nonadiabatic potential $V_{\rm na}(z)$. As a consequence, (i) the microscope resolution is unlimited at the level of the focusing function engineering and (ii) the nonadiabatic potential $V_{\rm na}(\hat{z})$ can be neglected in the SME (22) hereafter. However, with decreasing ϵ/β one also reduces the signal strength in the photocurrent which is proportional to the population of the $|r\rangle$ state such that a longer measurement time is required to distinguish it from the shot noise. The long measurement time in turn increases the role of spontaneous-emission processes which ultimately limit the microscope resolution, as discussed below in Sec. IV B 4.

We comment that, although we have focused here on a standing-wave implementation of the focusing function, there exist alternative designs of the laser profiles for dark-state microscopy, e.g., exploiting optical vortices created by holographic techniques or by Laguerre-Gaussian beams [15,20].

E. Filtered homodyne current and the SNR

In this section we discuss the signal filtering for homodyne detection and thus define the SNR, which will serve as a key figure of merit to quantify the performance of the microscope below.

The homodyne current [see e.g., Eq. (5) or (23)] is noisy, as it contains the (white) shot noise corresponding to the Wiener increment $dW(t)$, inherited from the vacuum fluctuation of the electromagnetic bath. The shot noise can be suppressed by filtering the homodyne current with a linear low-pass filter,

$$\mathcal{I}_\tau(t) = \int dt' h_\tau(t - t') I(t'). \tag{29}$$

Here $\mathcal{I}_\tau(t)$ is the filtered homodyne current, while $h_\tau(t)$ is the filter function with a frequency bandwidth characterized by $1/\tau$. The filter passes the low-frequency components of the homodyne current including the conditional expectation value $\sqrt{\kappa}\langle\hat{X}_\phi\rangle_c$ and attenuates the high-frequency component of the shot noise, reducing its variance to $\sim 1/\tau$. With diminished shot noise, the filtered homodyne current allows us to directly read out the signal which, as will be discussed in detail in Sec. IV, maps out the spatial density of the atomic system.

The quality of the filtered homodyne current is reflected by its SNR, i.e., the relative power between the signal and the noise, defined as

$$\mathrm{SNR}(t) = \frac{\langle\mathcal{I}_\tau(t)\rangle^2_{\rm st}}{\langle\mathcal{I}^2_\tau(t)\rangle_{\rm st} - \langle\mathcal{I}_\tau(t)\rangle^2_{\rm st}}, \tag{30}$$

where $\langle\cdots\rangle_{\rm st}$ denotes statistical averaging over all measurement runs. We note that on the right-hand side (RHS) of Eq. (30) the total noise variance (in the denominator) includes not only the filtered shot noise, but also the noise inherited from the fluctuating signal $\sqrt{\kappa}\langle\hat{X}_\phi\rangle_c$ [cf. Eqs. (5) and (29)]. This noise component is a manifestation of the measurement backaction.

Both the filtered homodyne current $\mathcal{I}_\tau(t)$ and its SNR depend on the choice of the filter function $h_\tau(t)$, in particular its inverse bandwidth τ. On the one hand, τ should be chosen as large as possible, to suppress the shot noise thus to enhance the SNR; on the other hand, τ should be kept small enough for the signal to pass through. The optimal τ will depend on the systems under observation and the operation modes of the microscope. This will be discussed in detail in Sec. IV. In contrast to the bandwidth, the exact shape of $h_\tau(t)$ has much smaller impact on both the filtered homodyne current and its SNR, and a simple filter suffices to illustrate the main features of the measured quantity. In this paper we adopt the filter

$$h(t) = \begin{cases} \tau^{-1} e^{-t/\tau}, & t \geqslant 0 \\ 0, & t < 0. \end{cases} \tag{31}$$

Besides its simplicity, it has the additional benefit that the corresponding SNR (30) can be calculated efficiently with a numerical method as detailed in Appendix B.

F. Summary of the model

The key result of the present section is the SME (22) describing the dynamics of the quantum scanning microscope, together with the corresponding homodyne current (i.e., the measurement signal) (23). Altogether, they allow us to study the various operation modes of the microscope and examine its performance in the presence of the atomic spontaneous emission, to be detailed in Sec. IV.

IV. MICROSCOPE OPERATION

With the quantum optical model at hand, we discuss below in detail the operation of the microscope. The microscope is characterized by three parameters: the spatial resolution $\sigma \ll \lambda_0$, the temporal resolution $\tau_c = 1/\kappa$, with κ the cavity linewidth, and the dispersive atom-cavity coupling $\mathcal{A}$ controlling the measurement strength [see Eq. (24)]. As we will show, the bad (good) cavity limit, defined as the cavity linewidth κ being much larger (smaller) than the frequency scale of atomic motion, corresponds to two operating modes of the microscope, which we call the movie mode and scanning mode, respectively. These operation modes feature distinct effective observables of the atomic system, thus providing different strategies for measuring the atomic density, with different applications.

In the following we explore these operating modes, by analyzing the observables being measured, and the corresponding measurement backaction. We illustrate these features via numerical simulation of the measurement for a simple example system, an atom moving in a harmonic oscillator (HO) potential $V(z) = m\omega^2 z^2/2$, with the atomic mass m, trap frequency ω, and motional eigenstates $|n\rangle$, $n = 0, 1, 2 \ldots$. For this system, the movie mode (scanning mode) is defined by $\kappa \gg \omega$ ($\kappa \ll \omega$). Further, to resolve the spatial density distributions, we require a spatial resolution better than the length scale $\ell_0 \equiv \sqrt{\hbar/m\omega}$ set by the HO ground state, $\sigma \lesssim \ell_0$. We include in this discussion decoherence due to spontaneous emission

as imperfection, aiming at providing a direct reference for experimental implementations of the microscope.

A. Bad cavity limit: Movie mode of the microscope

In the bad cavity limit the cavity dynamics is much faster than the atomic motion such that the former instantaneously follows the latter. Such a timescale separation allows us to adiabatically eliminate the cavity mode in Eqs. (22) and (23), resulting in an equation for the atomic density matrix $\tilde{\rho}_c \equiv \mathrm{Tr}_C(\rho_c)$ alone, where Tr_C indicates a trace over the cavity mode. Carrying out this elimination (see Appendix C) results in the expression for the homodyne current [see also Eq. (6)]

$$dq(t) \equiv I(t)dt = 2\sqrt{\gamma}\langle f_{z_0}(\hat{z})\rangle_c\, dt + dW(t), \tag{32}$$

i.e. the homodyne current directly reflects the expectation value of the focusing function $f_{z_0}(\hat{z})$. In Eq. (32)

$$\gamma = \left(\frac{4\mathcal{A}\mathcal{E}}{\hbar\kappa}\right)^2 \approx \left(4\mathcal{E}\mathcal{C}\frac{\sigma}{\ell_0}\frac{\Gamma_t}{\Delta_t}|\langle r|D(z)\rangle|^2_{\max}\right)^2 \tag{33}$$

is the measurement rate with $\mathcal{C} = g^2(z_0)/\kappa\Gamma_t$ the cavity cooperativity, and we have chosen the homodyne angle as $\phi = -\pi/2$ to maximize the homodyne current (see Appendix C). Correspondingly, the evolution of the atomic system is given by

$$\begin{aligned} d\tilde{\rho}_c = &-\frac{i}{\hbar}[\hat{H}_{A,E}, \tilde{\rho}_c]\,dt + \gamma\mathcal{D}\big[f_{z_0}(\hat{z})\big]\tilde{\rho}_c\,dt \\ &+ \sqrt{\gamma}\mathcal{H}\big[f_{z_0}(\hat{z})\big]\tilde{\rho}_c\,dW(t) + \frac{\gamma}{4\mathcal{C}}\mathcal{L}_{\mathrm{sp}}\tilde{\rho}_c\,dt. \end{aligned} \tag{34}$$

Here the first term on the RHS describes the coherent evolution of the atom according to its motional Hamiltonian $\hat{H}_{A,E}$, while the second and the third terms describe the backaction resulting from continuous measurement of $f_{z_0}(\hat{z})$. The last term corresponds to decoherence of the motional density matrix of the atom due to spontaneous emission,

$$\begin{aligned} \mathcal{L}_{\mathrm{sp}}\tilde{\rho}_c = &\mathcal{D}\big[f_{z_0}(\hat{z})\big]\tilde{\rho}_c + P_{re}\mathcal{D}\big[f_{z_0}(\hat{z})\sin\hat{\alpha}_{z_0}\big]\tilde{\rho}_c \\ &+ P_{ge}\mathcal{D}\big[f_{z_0}(\hat{z})\tan\hat{\alpha}_{z_0}\sin\hat{\alpha}_{z_0}\big]\tilde{\rho}_c - \tfrac{1}{2}\big\{f^2_{z_0}(\hat{z})\big[\tan^2\hat{\alpha}_{z_0} \\ &\times\big(1 - P_{ge}\sin^2\hat{\alpha}_{z_0}\big) - P_{re}\sin^2\hat{\alpha}_{z_0}\big], \tilde{\rho}_c\big\}, \end{aligned} \tag{35}$$

which will be analyzed in detail in Sec. IV A 2.

Equations (32) and (34) provide a complete description of the quantum evolution of the atom subjected to continuous measurement in the movie mode of the microscope. In the following we study the measurement and its backaction as well as effects of spontaneous emission, which we illustrate with the example of monitoring wave-packet dynamics in a harmonic oscillator potential.

1. Observable and the measurement backaction

The observable in the movie mode is the focusing function $f_{z_0}(\hat{z})$ [cf. Eq. (32)], which provides information of the local atomic density with a resolution σ [cf. Eq. (27)], where in the limit $\sigma \to 0$, $f_{z_0}(\hat{z}) \sim \delta(\hat{z} - z_0) = |z_0\rangle\langle z_0|$. Given that $f_{z_0}(\hat{z})$ does not commute with the Hamiltonian of the atomic system, $[\hat{H}_{A,E}, f_{z_0}(\hat{z})] \neq 0$, the movie mode is obviously not QND, i.e., measurement backaction competes with the coherent dynamics generated by $\hat{H}_{A,E}$.

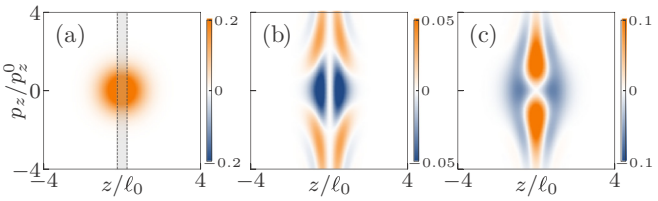

FIG. 4. Visualization of the effect of the measurement backaction in the movie mode of the microscope, via the Wigner function of (a) $\tilde{\rho}_c = |0\rangle\langle 0|$, (b) $\mathcal{D}[f_{z_0}(\hat{z})]\tilde{\rho}_c$, and (c) $\mathcal{H}[f_{z_0}(\hat{z})]\tilde{\rho}_c$, for an atom in a HO potential. The focal region is shown as the dashed area in (a), with focal point $z_0 = 0$ and resolution $\sigma = 0.5\ell_0$, where $\ell_0 \equiv \sqrt{\hbar/m\omega}$ is the HO length scale. Comparing (a) and (b), we see that the decoherence term $\mathcal{D}[f_{z_0}(\hat{z})]\tilde{\rho}_{\mathrm{th}}$ increases the momentum fluctuation of the atom. Comparing (a) and (c), we find that $\mathcal{H}[f_{z_0}(\hat{z})]\tilde{\rho}_{\mathrm{th}}$ induces a redistribution of the population between the focal region and the outside (see the text).

The measurement backaction is represented by terms $\mathcal{D}[f_{z_0}(\hat{z})]\tilde{\rho}_c$ and $\mathcal{H}[f_{z_0}(\hat{z})]\tilde{\rho}_c$ in Eq. (34). To visualize the action of these terms, we plot in Fig. 4 the corresponding Wigner functions in phase space, where we take the ground motional state $\tilde{\rho}_c = |0\rangle\langle 0|$ of the atom in the HO potential as the reference state [with the Wigner function plotted in Fig. 4 (a)]. As can be seen in Figs. 4(b) and 4(c), respectively, the decoherence term $\mathcal{D}[f_{z_0}(\hat{z})]$ induces momentum diffusion of the atom, while the homodyne term $\mathcal{H}[f_{z_0}(\hat{z})]$ continuously projects the atomic state inside and outside the focal region, by stimulating population flow between these two regions. Both terms elongate the Wigner function of the atom along p_z, manifesting the enhanced momentum fluctuation due to the measurement.

To visualize the competition between the measurement backaction and the Hamiltonian, we show in Fig. 5, for different times, the Wigner function of an atom in a coherent state evolving according to Eq. (34) and averaged over all measurement outcomes (i.e., as a solution of the quantum

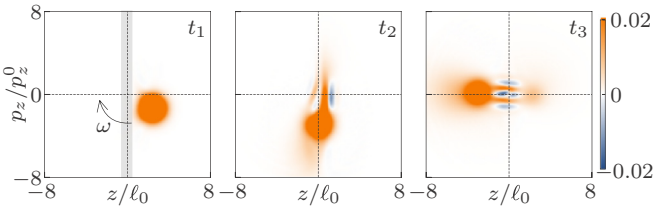

FIG. 5. Dynamics of the measurement in the movie mode of the microscope. We show the Wigner function of a coherent state $|\alpha\rangle$, evolving in time according to Eq. (34), and average over all measurement outcomes to yield a deterministic evolution. At $t_1 = 0.1T_{\mathrm{osc}}$ ($T_{\mathrm{osc}} \equiv 2\pi/\omega$) the coherent state has not yet entered the focal region (shown as the gray area) and remains an equal distribution of position and momentum uncertainty. At $t_2 = 0.25T_{\mathrm{osc}}$, as the coherent state crosses into the focal region (centered at $z_0 = 0$), the distribution begins to spread out along the p_z axis. At $t_3 = 0.5T_{\mathrm{osc}}$, the increased uncertainty is fed into the z axis, increasing the fluctuation of the measured homodyne current (see the text). The parameters are chosen as $\alpha = 2$, $\sigma = 0.5\ell_0$, and $\gamma = 4\omega$.

master equation), where for simplicity we set $\mathcal{L}_{\rm sp} = 0$ in Eq. (34). As the atom passes through the focal region (here fixed at $z_0 = 0$), its momentum fluctuation is increased due to the measurement backaction, causing its Wigner function to spread out along the p_z axis (cf. Fig. 5 at time t_2). At later times, the Wigner function, now including the spread in momentum, continues to rotate with frequency ω, thus leading to extra fluctuation along z (cf. Fig. 5 at time t_3). The pattern appearing near the focal region in Figs. 5(b) and 5(c) results from the coherent interference between the transmitted component and the reflected component of the atomic wave packet when crossing the dissipative barrier in the focal region.

2. *Decoherence due to spontaneous emission*

Spontaneous emission induces extra decoherence in atomic motion, captured by Eq. (35). This term is derived from $\mathcal{L}'$ of Eq. (22) [given in Eq. (A23)]. The first three terms of Eq. (35) describe the momentum diffusion of the atomic wave packet in the focal region during the excitation–spontaneous-emission cycle involving the states $|t\rangle$ and $|r\rangle$. The last term of Eq. (35) describes the gradual loss of atoms due to the decay from the bright states $|\pm\rangle$ to levels lying outside the four-level system under consideration (see Fig. 11), which makes atoms invisible to the microscope. Altogether, these decoherence processes are strongly suppressed for cavities with high cooperativity, since their rate is given by $\gamma/4\mathcal{C}$ [cf. Eq. (34)].

To quantitatively understand the role of these extra decoherence processes, below we perform numerical simulation of the evolution of the atomic system subjected to continuous measurement and spontaneous emission, where the measurement rate γ and cooperativity $\mathcal{C}$ are chosen according to realistic experimental parameters (given in Sec. V). The simulations confirm that the atomic spontaneous emission introduces negligible detriment to the performance of the microscope for $\mathcal{C} \gg 1$, which can be achieved in state-of-the-art cavity QED experiments [27].

3. *Application: Monitoring wave-packet oscillations*

We demonstrate the movie mode of the microscope, as monitoring the oscillation of an atomic wave packet released in a HO potential. As shown below, the bad cavity condition $\kappa \gg \omega$ provides the time resolution to take a movie of time-dependent density distributions. This is accompanied, due to the non-QND nature of the measurement, by the competition between Hamiltonian dynamics and measurement backaction and as a consequence by limitations due to achievable SNR in a single measurement run.

We initialize the atom in a coherent state $|\alpha\rangle$ and monitor its subsequent oscillations by focusing the microscope at the trap center $z_0 = 0$. Without coupling to the microscope, the atomic wave packet will pass through the trap center with a velocity $v = \sqrt{2}\ell_0|\alpha|\omega$ at times $t = 1/4T_{\rm osc}, 3/4T_{\rm osc}, \ldots$, where $T_{\rm osc} \equiv 2\pi/\omega$ is the oscillation period. Once coupled to the microscope, the atom will evolve according to Eq. (34), characterized by a competition between free oscillation and measurement backaction. Such a competition is necessarily reflected in the measurement records of the microscope. To show this, in Fig. 6(a) we plot, for different measurement strengths γ, the ensemble-averaged homodyne current $\langle I(t)\rangle_{\rm st}$,

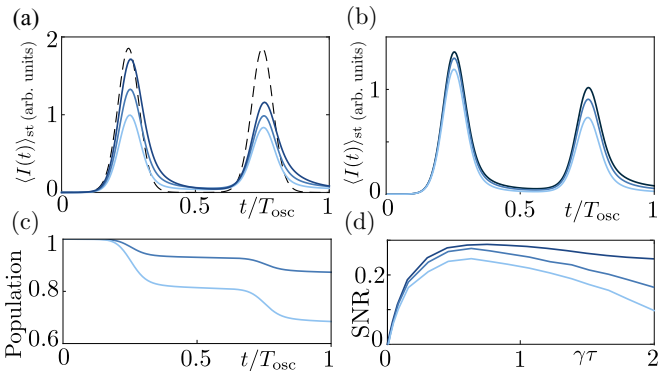

FIG. 6. Monitoring wave-packet oscillations in the movie mode of the microscope. (a) Statistically averaged homodyne current $\langle I(t)\rangle_{\rm st}$ over the oscillation period $T_{\rm osc} \equiv 2\pi/\omega$ with increasing measurement rate $\gamma = 1, 2, 4\omega$ (light to dark) and without spontaneous emission (corresponding to $\mathcal{C} = \infty$). The dashed line indicates the ideal transit signal with no measurement backaction (arbitrary unit). (b) $\langle I(t)\rangle_{\rm st}$ for $\gamma = 2\omega$, and $\mathcal{C} = 3, 10, \infty$ (light to dark). Lower $\mathcal{C}$ corresponds effectively to stronger spontaneous emission, which degrades the homodyne current. (c) Decay of the dark-state population due to spontaneous emission, with the same parameters as in (b). (d) SNR at the first peak ($t = 0.25T_{\rm osc}$) for a single measurement run, as a function of $\gamma\tau$, with τ the filter integration time (see the text), for $\mathcal{C} = 3, 10, \infty$ (light to dark).

with $I(t)$ given by Eq. (32) and $\langle\cdots\rangle_{\rm st}$ standing for statistical average. As can be seen clearly, $\langle I(t)\rangle_{\rm st}$ represents faithfully the shape of the atomic wave packet passing through the focusing region and reflects the measurement backaction as a successive distortion of the signal with time, which becomes more significant with increasing γ. The impact of atomic spontaneous emission is illustrated in Fig. 6(b), where we plot $\langle I(t)\rangle_{\rm st}$ for different strengths of spontaneous emission $\gamma/4\mathcal{C}$ at a fixed measurement strength γ. As shown there, spontaneous emission diminishes the measured homodyne current: The smaller the $\mathcal{C}$, the weaker the homodyne current. This is a direct consequence of the gradual depletion of the population in the internal dark state due to spontaneous emission, shown in Fig. 6(c).

The fact that the measurement backaction competes with the Hamiltonian evolution provides a limitation on the achievable SNR of the filtered homodyne current in a single measurement run. To illustrate this, we plot in Fig. 6(d) the SNR of a single measurement run against the dimensionless measurement strength $\gamma\tau$, where τ is the filter integration time (cf. Sec. III E). We choose an optimal τ defined via $\tau = \sigma/v$, with σ the microscope resolution and v the group velocity of the atomic wave packet at $z = 0$. It allows the signal (which has a bandwidth $\sim v/\sigma$ due to the finite resolution σ of the focusing function) to pass through while filtering out the shot noise with frequencies outside the defined bandwidth. In Fig. 6(d), at small measurement strength γ, the SNR grows with γ, due to the enhancement of the signal relative to the shot noise. At large γ, SNR eventually drops down because of the strong measurement backaction. The appearance of such an upper bound of the SNR in a single measurement run is a general feature of non-QND measurements [30]. Figure 6(d) also includes the effect of the atomic spontaneous emission.

As expected, spontaneous emission reduces the SNR further, since it diminishes the measured signal [cf. Fig. 6(b)].

B. Good cavity limit: Scanning mode of the microscope

We now consider the good cavity limit $\kappa \ll \omega$ where, as mentioned in Sec. II, the cavity effectively filters out the fast dynamics of the atomic system. This can be seen by transforming the SME (22) to an interaction picture with respect to $\hat{H}_{A,E}$, the motional Hamiltonian of the atom. In this picture the focusing function $f_{z_0}(\hat{z})$ becomes time dependent and can be expanded as $\sum_\ell \hat{f}^{(\ell)}_{z_0} e^{-i\ell\omega t}$, with the ℓth sideband component $\hat{f}^{(\ell)}_{z_0} \equiv \sum_n f_{n,n+\ell}|n\rangle\langle n+\ell|$ and $f_{mn} \equiv \langle m|f_{z_0}(\hat{z})|n\rangle$. Due to the narrow cavity linewidth $\kappa \ll \omega$, the cavity will effectively enhance the light coupling to the zero-frequency component $\hat{f}^{(0)}_{z_0}$ by averaging out the rest of $\hat{f}^{(\ell)}_{z_0}$ with $\ell \neq 0$. Consequently, only $\hat{f}^{(0)}_{z_0}$ is reflected in the homodyne current. As will be detailed in Sec. IV B 1, the operator $\hat{f}^{(0)}_{z_0}$ serves as an emergent QND (eQND) observable of the atomic density, which allows for mapping out the spatial density of energy eigenstates of the atom in a single measurement run with a high SNR.

In the good cavity limit, we can again eliminate the cavity mode to obtain equations of motion for the atomic system alone, the detailed derivation of which is presented in Appendix C. Summarizing the results, the expression for the homodyne current is given by [see also Eq. (7)]

$$dq(t) = I(t)dt = 2\sqrt{\gamma}\left\langle \hat{f}^{(0)}_{z_0}\right\rangle_c dt + dW(t). \tag{36}$$

We see, as mentioned above, the homodyne current following the expectation value of the eQND variable $\hat{f}^{(0)}_{z_0}$. Correspondingly, the evolution of the atomic system becomes

$$\begin{aligned} d\tilde{\rho}_c = &-\frac{i}{\hbar}[\hat{H}_{A,E}, \tilde{\rho}_c]\,dt + \sum_{\ell\neq 0}\frac{\gamma}{1+(2\omega\ell/\kappa)^2}\mathcal{D}\big[\hat{f}^{(\ell)}_{z_0}\big]\tilde{\rho}_c\,dt \\ &+\gamma\mathcal{D}\big[\hat{f}^{(0)}_{z_0}\big]\tilde{\rho}_c\,dt + \sqrt{\gamma}\mathcal{H}\big[\hat{f}^{(0)}_{z_0}\big]\tilde{\rho}_c\,dW(t) \\ &+\frac{\gamma}{4\mathcal{C}}\mathcal{L}_{\rm sp}\tilde{\rho}_c dt. \end{aligned} \tag{37}$$

Here γ is the measurement strength defined by Eq. (33) and $\mathcal{L}_{\rm sp}$ describes the extra decoherence introduced by atomic spontaneous emission [cf. Eq. (35)]. In Eq. (37), the superoperator for homodyne measurement contains only $\hat{f}^{(0)}_{z_0}$, while higher sideband components $\hat{f}^{(\ell)}_{z_0}$ with $\ell \neq 0$ only induce decoherence captured by the Lindblad operators $\mathcal{D}[\hat{f}^{(\ell)}_{z_0}]$, with a diminished rate $\gamma[1+(2\omega\ell/\kappa)^2]^{-1} \to 0$ as suppressed by the cavity in the limit $\kappa/\omega \to 0$. This fact causes distinct measurement backaction to the atomic system compared to the bad cavity limit in Sec. IV A, as will be discussed in detail below.

1. Emergent QND measurement of atomic density

In Ref. [1] we introduced the concept of eQND measurement, applicable to an arbitrary observable $\hat{\mathcal{O}}$ which, in general, does not necessarily commute with the Hamiltonian of the system. We define for $\hat{\mathcal{O}}$ a corresponding emergent QND observable as

$$\hat{\mathcal{O}}_{\rm eQND} \equiv \sum_n |n\rangle\langle n|\,\hat{\mathcal{O}}\,|n\rangle\langle n|\,, \tag{38}$$

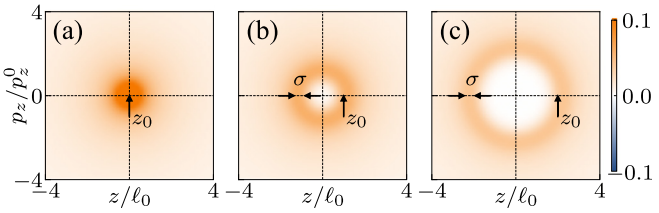

FIG. 7. The eQND observable $\hat{f}^{(0)}_{z_0}$ in the scanning mode of the microscope. We show the Wigner function of $\hat{f}^{(0)}_{z_0}$ for three different focal points (a) $z_0 = 0$, (b) $z_0 = \ell_0$, and (c) $z_0 = 2\ell_0$, with ℓ_0 the HO length scale. In (b) and (c), the Wigner function manifests as a doughnut centered on the origin, of radius z_0 and of width σ. The resolution $\sigma = 0.5\ell_0$.

with $|n\rangle$ energy eigenstates. Measurement of $\hat{\mathcal{O}}_{\rm eQND}$ provides the same information as of $\hat{\mathcal{O}}$ for the energy eigenstates, but in a nondestructive way.

Following this definition, we immediately see that $\hat{f}^{(0)}_{z_0}$ is the eQND observable corresponding to $\hat{f}_{z_0}(\hat{z})$. In particular, in the limit $\sigma \to 0$, we have $f_{z_0}(\hat{z}) \sim |z_0\rangle\langle z_0|$ such that $\hat{f}^{(0)}_{z_0} \sim \sum_n |\langle n|z_0\rangle|^2\,|n\rangle\langle n|$ directly provides the spatial density of energy eigenstates at the focal point z_0. Since $[\hat{f}^{(0)}_{z_0}, \hat{H}_{A,E}] = 0$, this measurement is nondestructive.

To gain an intuition of the backaction associated with this eQND measurement, in Fig. 7 we plot the Wigner function of $\hat{f}^{(0)}_{z_0}$, which shows a symmetric distribution around the phase-space center with a finite spread $\sim\sigma$. As such, continuous measurement of $\hat{f}^{(0)}_{z_0}$ does not lead to momentum diffusion. Rather, as in the familiar QND measurement [24–28], it reduces the coherence between different energy eigenstates and selects out a particular energy eigenstate. This is illustrated in Fig. 8, where we show the effect of the homodyne term $\mathcal{H}[f_{z_0}(\hat{z})]$ acting on a thermal state of the atom in a HO potential, which induces redistribution of the population of motional eigenstates. Moreover, depending on the focal point z_0, the measurement backaction mainly changes the population of a particular eigenstate $|n\rangle$ with the largest matrix element $\langle n|f_{z_0}(\hat{z})|n\rangle$. This can be clearly seen by comparing Figs. 8(a)–8(c).

The eQND measurement shares the same merit as the standard QND measurement [30]: Once the atomic state is projected onto an energy eigenstate, the only noise source in

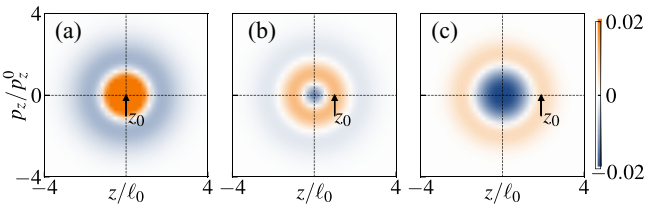

FIG. 8. Measurement backaction in the scanning mode of the microscope. We choose $\sigma = 0.5\ell_0$ and plot the Wigner function of $\mathcal{H}[f_{z_0}(\hat{z})]\bar{\rho}_{\rm th}$ for a thermal state $\bar{\rho}_{\rm th} = \sum_n p_n\,|n\rangle\,\langle n|$ of a HO, with $p_n \propto e^{-n/n_{\rm th}}$ and $n_{\rm th} = 1$, for focal points (a) $z_0 = 0$, (b) $z_0 = \ell_0$, and (c) $z_0 = 2\ell_0$. The Wigner function shows a density flow in the phase space, corresponding to a redistribution of the population of the energy eigenstates (see the text).

the measured homodyne current is the photon shot noise, which can be made arbitrarily small by increasing the measurement strength γ (or, equivalently, the measurement time). The extra decoherence terms in Eq. (37) introduce slight imperfections to this ideal scenario. These include $\mathcal{D}[\hat{f}^{\ell}_{z_0}]$, $\ell \neq 0$, which describes incoherent quantum jumps between energy eigenstates, and the spontaneous-decay term $\mathcal{L}_{\rm sp}$ qualitatively analyzed in Sec. IV A 2. The presence of these imperfections introduces extra noise to the homodyne current, thus reducing its SNR. Nevertheless, the features of the eQND measurement, in particular the ability to map out the spatial density of energy eigenstates with a high SNR in a single measurement run, is robust against these imperfections, as we show below.

2. Stochastic rate equation

To provide a physical interpretation for the dynamics of eQND measurement and the impact of imperfections, let us expand Eq. (37) in the energy eigenbases and obtain a (nonlinear) stochastic rate equation (SRE) for the eigenstate populations $p_n \equiv \langle n|\tilde{\rho}_c|n\rangle$:

$$dp_n = \sum_{\ell\neq 0} A^{\ell}_n (p_{n+\ell} - p_n)dt - B_n p_n\, dt + 2\sqrt{\gamma}\, p_n \left(f_{nn} - \sum_m f_{mm} p_m \right) dW(t). \tag{39}$$

Here we have defined the rates

$$A^{\ell}_n \equiv \left[\frac{\gamma}{1+(2\ell\omega/\kappa)^2} + \frac{\gamma}{4\mathcal{C}} \right] |f_{n,n+\ell}|^2, \tag{40}$$

$$B_n \equiv \frac{\gamma}{4\mathcal{C}} \langle n|\, f^2_{z_0}(\hat{z}) \left[\frac{\Omega_r(\hat{z})}{\Omega_g} \right]^2 |n\rangle \tag{41}$$

and have dropped small terms proportional to $P_{re\,(ge)}$ as well as the fast-rotating terms in $\mathcal{L}_{\rm sp}$.

The effect of the measurement is captured by the stochastic term in the second line of Eq. (39). It describes the collapse of the motional density matrix of the atom to a particular energy eigenstate $\tilde{\rho}_c(t) \to |n\rangle\langle n|$ within a collapse time $T_{\rm coll} \sim 1/\gamma$. The impact of higher sideband transitions and the atomic spontaneous emission is contained in the first line of Eq. (39). Here the first term describes redistribution of the population between the energy eigenstates, which preserves the total population $\sum_n p_n$. In the limit of $\kappa/\omega \ll 1$ and $\mathcal{C} \gg 1$ this process happens on a much longer timescale, the dwell time $T_{\rm dwell} \sim [\gamma/4\mathcal{C} + \gamma(\kappa/2\omega)^2]^{-1} \gg T_{\rm coll}$. The second term describes the decay of the population of the motional eigenstates due to spontaneous emission. It also happens on a much longer timescale $T_{\rm sp} \sim \gamma/4\mathcal{C} \gg T_{\rm coll}$.

As a result, the evolution of the atomic system corresponding to Eq. (39) consists of a rapid collapse to an energy eigenstate $|n\rangle$, followed by a sequence of rare quantum jumps between the energy eigenstates on the timescale $T_{\rm dwell}$ or loss of the atom on the timescale $T_{\rm sp}$. Such a timescale separation allows us to define a time window $T_{\rm coll} \ll T \lesssim T_{\rm dwell}, T_{\rm sp}$, during which the information of the energy eigenstates can be extracted backaction-free. This enables the scanning mode of the microscope, as discussed in the following.

3. Application: Preparing and scanning motional eigenstates

The scanning mode operates by moving the focal point $z_0(t)$ across the atomic system, $-L/2 < z_0(t) < L/2$, during a time T satisfying $T_{\rm coll} \ll T \lesssim T_{\rm dwell}, T_{\rm sp}$. By starting the scan, the motional state of the atom will first collapse to a particular energy eigenstate $|n\rangle$ (note that this stage can be viewed as state preparation), with the subsequent scan reading out the spatial density profile $\langle n|\hat{f}^{(0)}_{z_0}|n\rangle = \int dz\, f_{z_0}(z)|\langle z|n\rangle|^2$, until the atom jumps to another energy eigenstates or gets lost due to spontaneous decay.

As an illustration, we consider the scan of an atom trapped in a HO potential. To this end, we choose $\omega/\kappa = 10$ and assume that the atom is prepared at $t = 0$ in a thermal motional state of the HO potential $\tilde{\rho}(0) = \tilde{\rho}_{\rm th} = \sum_n p_n |n\rangle\langle n|$, with $p_n \propto e^{-n/n_{\rm th}}$ and $n_{\rm th} = 1$. In our illustration, we perform three consecutive spatial scans covering $-L/2 < z_0(t) < L/2$ ($L = 8\ell_0$), each for a time interval T ($\gamma T = 1000$). In Fig. 9(a) we show the resulting homodyne current and the corresponding population of the energy eigenstates in a single run, based on integrating the SRE (39). In filtering the homodyne current, we choose the optimal filter time $\tau = \sigma/v$, with σ the microscope resolution and $v = L/T$ the scanning speed. As can be seen in Fig. 9(a), in scan 1 the microscope prepares the atom in a particular energy eigenstate (here the first excited state $|1\rangle$) in a random way according to the initial-state distribution. The atom stays in $|1\rangle$ in scan 2, allowing for a faithful readout of its spatial density through the detected homodyne current. In scan 3 the atom stays in $|1\rangle$ until it suddenly gets lost due to spontaneous decay out of its internal dark state, manifesting in the homodyne current as a sudden jump to zero. Such a loss event is fast (on a timescale $\sim T_{\rm coll}$) but rare (on a timescale $\sim T_{\rm sp}$ after the beginning of scan). In Fig. 9(b) we show another simulation of Eq. (39) representing another independent measurement run. In this run the microscope prepares the atom in the motional ground state $|0\rangle$ in scan 1 and subsequently reveals its spatial density in scan 2. However, in scan 3 of Fig. 9(b), the atom first stays in $|0\rangle$ and then instead of disappearing suddenly jumps to the second excited state $|2\rangle$, with the homodyne current starting tracing the density profile of $|2\rangle$. Such a quantum jump is induced by the higher sideband transition terms $\mathcal{D}[\hat{f}^{\ell}_{z_0}]$, $\ell \neq 0$. It is fast (on a timescale $\sim T_{\rm coll}$) but rare ($\sim T_{\rm dwell}$ between adjacent jumps).

To quantify the performance of the scanning microscope in the presence of imperfections, we plot in Fig. 9(c) the SNR of a single scan of a motional eigenstate of the atom as a function of the (dimensionless) measurement strength γT for different ω/κ and different cooperativity $\mathcal{C}$. The solid curves reflects the effect of higher sideband transitions $\mathcal{D}[\hat{f}^{\ell}_{z_0}]$ in Eq. (37), with $\mathcal{L}_{\rm sp} = 0$. As can be seen, for small γ the SNR increases with γ linearly (i.e., in a QND fashion). For large γ, however, the SNR deviates from linear increase due to these higher sidebands transitions. By increasing ω/κ we greatly suppress these processes, rendering them into rarer quantum jumps, thus improving the SNR. The effect of atomic spontaneous decay is shown as the dashed curves in Fig. 9(c), where we plot the behavior of the SNR for different $\mathcal{C}$ while keeping ω/κ fixed. As expected, spontaneous decay degrades the achievable SNR, as it brings the atomic population out of the dark state. This effect is however strongly suppressed for large $\mathcal{C}$.

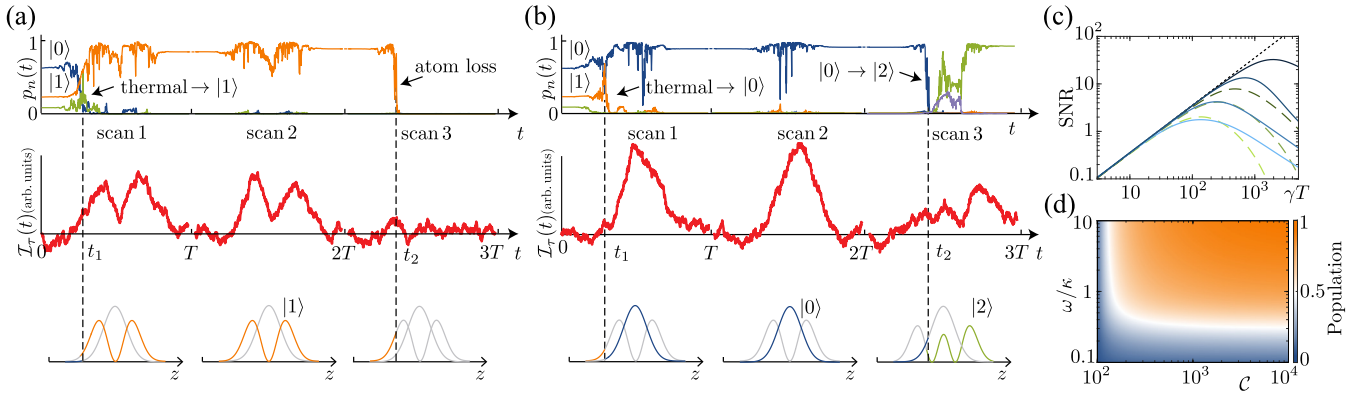

FIG. 9. Single-run scans in the scanning mode of the microscope. (a) and (b) Simulation of two independent measurement runs for an atom initialized in a thermal state of a HO with $n_{\rm th} = 1$ (see the text). Each measurement run consists of three consecutive scans, where the focal point is moved across the atomic system in a time T. The conditional populations $p_n(t)$ $(n = 0, 1, 2)$ of the energy eigenstates (top panel) and the filtered homodyne current $\mathcal{I}_\tau(t)$ (middle panel) are shown together with the spatial density inferred from the trap populations (bottom panel). The eQND measurement prepares the atom in a trap eigenstate [$|1\rangle$ in (a) and $|0\rangle$ in (b)] at a time labeled by t_1 in the first scan $t \in [0, T]$, and $\mathcal{I}_\tau(t)$ traces the corresponding density faithfully in the second scan $t \in [T, 2T]$. In (a), the atom is lost at a time $t_2 \in [2T, 3T]$ due to spontaneous decay, whereas in (b), the atom jumps to the trap state $|2\rangle$ at $t_2 \in [2T, 3T]$. The parameters are $\gamma T = 1000$, $\mathcal{C} = 200$, and $\sigma = 0.5\ell_0$. (c) SNR vs γT for a single scan of an atom initialized in the eigenstate $|1\rangle$ of the HO, compared to an ideal QND measurement (42) (dotted straight line), for $\sigma = 0.5\ell_0$. The SNR is taken at $z_0(t) = -\ell_0$ (theoretical maximum). Solid curves show $\omega/\kappa = 10, 4, 1, 0.1$ (dark to light), assuming no spontaneous emission (i.e., $\mathcal{C} = \infty$). Dashed curves show $\mathcal{C} = 1000, 200, 100$ (dark to light) and $\omega/\kappa = 10$. (d) For an atom initialized in $|1\rangle$, we plot its final population in $|1\rangle$ after completing a single scan, averaged over all measurement outcomes. We choose $\gamma T = 1000$ and $\sigma = 0.5\ell_0$. Increasing ω/κ and improving $\mathcal{C}$ greatly suppresses the population depletion.

As another indicator of the microscope performance, we plot in Fig. 9(d) the remaining population of an initially populated motional eigenstate after completing a single scan, averaged over all measurement runs. As can be seen, in the regime $\kappa \ll \omega$ and $\mathcal{C} \gg 1$, the population remains around 1, indicating a nearly ideal eQND measurement.

To summarize, Fig. 9 demonstrates that by taking a good cavity $\kappa \ll \omega$ and choosing sufficiently large cooperativity $\mathcal{C} \gg 1$ to suppress the atomic spontaneous emission, the scanning mode of the microscope is able to map out the spatial density of energy eigenstates with a high SNR in a single scan as an eQND measurement.

4. Resolution limit of the microscope

As it was already mentioned in Sec. III D, the spatial resolution of the microscope is limited by the spontaneous-decay processes leading to the loss of an atom. In this section we estimate analytically and evaluate numerically the effect of the spontaneous emission on the SNR in the scanning mode, as a function of the resolution σ.

In the limit of high spatial resolution $\sigma \ll \ell_0$, with ℓ_0 being the characteristic length of the atomic wave function, the focusing function $f_{z_0}(z)$ has the form of a narrow peak with the height $\sim\ell_0/\sigma$ and the width $\sim\sigma$ around z_0. After assuming that the system during the scan has already collapsed to an eigenstate $|n\rangle$ and averaging the photocurrent in Eq. (36) over the time window $\tau = T\sigma/L$, we obtain an estimate for the SNR limited by the shot noise

$$\mathrm{SNR}(z_0, T) \simeq 4\gamma T \frac{\sigma}{L} |\tilde{\psi}_n(z_0/\ell_0)|^4, \tag{42}$$

where we define the dimensionless wave function $\tilde{\psi}_n(z_0/\ell_0) = \sqrt{\ell_0}\,\langle n|z_0\rangle$. The linear dependence of the SNR on the total scan time T is shown as a dotted line in Fig. 9(c). However, for long enough T, the decoherence processes become important and result in the deviation from the linear dependence. In the limit $\sigma \ll \ell_0$, the corresponding timescale is defined by the B_n terms in Eq. (39), which, following Eq. (41), can be estimated as

$$B_n(z_0) \sim \frac{\gamma}{\mathcal{C}} \frac{E_r}{V_{\rm na}^{\max}} \frac{\ell_0}{k_0^2\sigma^3} |\tilde{\psi}_n(z_0/\ell_0)|^2.$$

The terms A_n^ℓ can be neglected because the matrix elements $|f_{nm}|$ are of order 1 for any σ and therefore $A_n^\ell \ll B_n$ for $\sigma \ll \ell_0$ and $\omega/\kappa \gg 1$. As a result, for the total scan over the distance L during the time T, the atom loss probability reads

$$\tilde{B}_n T \sim \frac{\gamma T}{\mathcal{C}} \frac{E_r}{V_{\rm na}^{\max}} \frac{1}{k_0^2\sigma^3} \frac{l_0^2}{L}, \tag{43}$$

where $\tilde{B}_n = L^{-1} \int B_n(z_0) dz_0$ is the spatial average. For $\tilde{B}_n T \ll 1$, the atom loss can be neglected and the SNR grows linearly with T following Eq. (42). For longer T, however, the atom can eventually be lost with the result that the average photocurrent drops to zero, which we regard as a noise. Therefore, after taking the effect of the atomic spontaneous decay into account, the SNR can be written as

$$\mathrm{SNR}(z_0, T) \simeq \frac{4\gamma T \frac{\sigma}{L} |\tilde{\psi}_n(z_0/\ell_0)|^4}{1 + 4\gamma T \frac{\sigma}{L} |\tilde{\psi}_n(z_0/\ell_0)|^4 \tilde{B}_n T}, \tag{44}$$

which is in a good agreement with the dashed lines in Fig. 9(c) that represent the direct numerical simulations of Eq. (39).

By evaluating the SNR at the maximum of the wave function and optimizing it over the measurement time T in Eq. (44), we

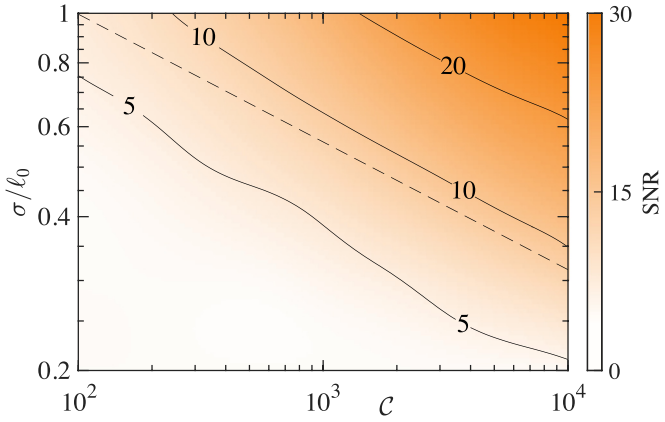

FIG. 10. Resolution limit of the microscope. The relation between the cavity cooperativity $\mathcal{C}$, the spatial resolution σ (in units of the HO length $\ell_0 \equiv \sqrt{\hbar/m\omega}$), and the maximally achievable SNR for a single scan of an atom initialized in $|1\rangle$ of a HO potential (SNR is calculated for the maximum of the wave function at $z_0(t) = -\ell_0$ and optimized over γT) is shown. The parameters are $\omega/\kappa = 10$ and $V_{\rm na}^{\rm max} = 0.1\hbar\omega$. The dashed line shows the scaling $\sigma/\ell_0 \sim \mathcal{C}^{-1/4}$ according to Eq. (45) for a fixed SNR.

obtain a universal expression

$$\left(\frac{\sigma}{\lambda_0}\right)_{\rm min} \sim \left(\frac{\rm SNR^2}{\mathcal{C}}\frac{E_r}{V_{\rm na}^{\rm max}}\frac{\ell_0^2}{\lambda_0^2}\right)^{1/4} \tag{45}$$

for the resolution limit of the microscope. The corresponding optimal measurement time is given by $\gamma T \sim k_0\sigma(L/\ell_0)\sqrt{\mathcal{C}\,V_{\rm na}^{\rm max}/E_r}$. It follows from Eq. (45) that the spatial resolution is limited by the cavity cooperativity $\mathcal{C}$ and by the chosen SNR (of a single measurement run). Improving the resolution leads to reducing the SNR, which, however, can be compensated by increasing the cavity cooperativity $\mathcal{C}$ to suppress the atomic spontaneous emission. Figure 10 shows the relation between the maximally achievable SNR, the spatial resolution, and the cavity cooperativity, calculated from numerical simulation of Eq. (39) for the case of the harmonic oscillator, which is in good agreement with the scaling behavior predicted by Eq. (45).

V. EXPERIMENTAL FEASIBILITY

We now address the experimental feasibility of the quantum scanning microscope. As we will show below, the present state-of-the-art experiments provide all the necessary ingredients for realization of the microscope itself and both operation modes.

First of all, the proposed setup for quantum scanning microscope requires trapping of atoms inside a high-Q optical cavity, which has already been realized in several experimental platforms ranging from cold neutral atoms in optical traps (lattices) [31] to trapped ions [32]. Another ingredient, the homodyne detection, is a well-developed technique that can be performed with nearly unit efficiency [33]. An implementation of the subwavelength focusing function via the dark-state engineering in an atomic Λ configuration (cf. Fig. 1) also looks realistic in view of the recent experimental realization [34] of the subwavelength optical barriers and the possibility to shine additional lasers from the side as was done in [35].

The movie mode of the microscope (Sec. IV A) requires the bad cavity condition $\kappa \gg \omega$. In fact, this is the typical situation for cavity QED experiments with optically trapped neutral atoms (see, e.g, Ref. [31]), where the cavity linewidth κ, on the order of megahertz, is much larger than the frequency of the atomic motion $\omega \sim E_r/\hbar$, on the order of kilohertz.

The scanning mode (Sec. IV B) needs a good cavity with $\kappa \ll \omega$. This condition can be met in cavity QED setups with optically trapped neutral atoms. For example, Ref. [36] reports strong coupling between an atomic BEC with a narrow linewidth optical cavity with $\kappa \simeq 2\pi \times 4.5$ kHz, far smaller than the optical recoil energy for light-mass alkali-metal atoms (e.g., $E_r/\hbar \simeq 2\pi \times 23$ kHz for ^{23}Na at the $D2$ line with $\lambda_0 \simeq 590$ nm). Ions trapped in optical cavities [35] provide another feasible platform for reaching the good cavity condition due to their large oscillation frequency (ω on the order of megahertz).

The spontaneous emission, as discussed in Sec. IV A 2, degrades the measured homodyne current due to gradual depletion of the atom from the dark state. This detrimental effect can be strongly suppressed by using high-Q optical cavities with large cooperativity (e.g., $\mathcal{C} > 100$ in Ref. [37]).

For a concrete illustration, we consider the example of a single ^{23}Na atom trapped in an optical lattice with the amplitude $V_0 = 5E_r$, where $E_r/\hbar \simeq 2\pi \times 23$ kHz, which corresponds to the harmonic oscillator frequency $\omega = \sqrt{2V_0E_r}/\hbar \simeq 2\pi \times 76$ kHz and the size of the ground state $\ell_0 = \sqrt{\hbar/m\omega} \simeq 75$ nm. For the focusing function we choose $\epsilon = \beta/3 = 0.1$, which leads to a resolution [see Eq. (27)] $\sigma \simeq 0.07\lambda_0 \simeq 0.5\ell_0$ and $V_{\rm na}^{\rm max} \simeq 0.1\hbar\omega$ [see Eq. (28)] being much smaller than the level spacing in the trap. For a cavity with the cooperativity $\mathcal{C} = 200$ we have for the spontaneous emission rate $\sim\gamma/4\mathcal{C} \ll \gamma$, which is negligible for the movie mode (cf. Fig. 6) and provides high enough SNR (cf. Fig. 9) to map out the atomic density distribution in a single experimental run in the scanning mode.

VI. CONCLUSION AND OUTLOOK

We have presented a detailed theoretical description of the quantum scanning microscope for cold atoms in the CQED setup proposed in [1] and discussed its experimental feasibility. The microscope is conceptually different from the familiar destructive microscopes in cold-atom experiments by allowing a continuous monitoring of an atomic system with optical subwavelength spatial resolution and by demonstrating the nondemolition observation of the atomic density operator as an emergent QND measurement. The concept of the emergent QND measurement extends the notion of the backaction-free continuous measurement to the case of a general quantum mechanical observable monitored in a system energy eigenstate.

Furthermore, we have demonstrated the action of the microscope as a device for continuous observation with two examples illustrating the two different operation modes: the observation of the atomic wave packet moving in a harmonic trap through the fixed focal region (the movie mode) and a scan of the atomic density distribution in a motional eigenstate of a harmonically trapped atom by moving the focal region slowly across the trap (the scanning mode). In the latter case, the microscope can be used for a probabilistic preparation of the atomic system in a pure motional eigenstate starting from an initial mixed one as a result of the measurement induced

state collapse. These examples demonstrate the fundamental difference in the action of the proposed microscope allowing continuous observation of a quantum system from the common measurement scenario with the quantum gas microscope where a single shot destructive measurement terminates a given run of the experiment.

We also mention that the ideas behind the microscope operation and the emergent QND measurement are not necessarily restricted to CQEDs implementation considered here, but can be realized with other experimental platforms, e.g., coupling the atom of interest to an ensemble of Rydberg atoms for readout. Finally, we emphasize that continuous observation of a quantum system provides the basis of a quantum feedback [4] on the system of interest, which is of particular interest for quantum many-body systems.

ACKNOWLEDGMENTS

We acknowledge J. Reichel for fruitful discussions and comments. Some of the numerical simulations were performed using the QuTiP library [38]. Work at Innsbruck was supported by the Austrian Science Fund SFB FoQuS (FWF Project No. F4016-N23) and the European Research Council Synergy Grant UQUAM.

APPENDIX A: DETAILS OF THE ADIABATIC ELIMINATION OF THE ATOMIC INTERNAL DYNAMICS

In this Appendix we present details of the adiabatic elimination of the atomic internal DOFs, which is sketched briefly in Sec. III C of the main text. As described in Sec. III C, we are interested in the regime where (i) the external motion of an atom is much slower than its internal dynamics, $|\hat{H}_{A,E}| \ll |\hat{H}_{A,I}|$, and (ii) the atom is coupled to the cavity mode dispersively, $g(z) \ll \Delta_t$. Condition (i) allows us to define a small parameter $\varepsilon_1 = \mathrm{Tr}(\mu_c \hat{H}_{A,E})/\hbar\Omega(z)$, where μ_c is the density matrix for the joint atom-cavity system introduced in Sec. III B and $\Omega(z) \equiv \sqrt{\Omega_g^2 + \Omega_r^2(z)}$ characterizes the energy gap between the internal dark and bright states. Condition (ii) allows us to define another small parameter $\varepsilon_2 = \mathrm{Tr}(\mu_c \hat{H}_{AC})/\hbar\Delta_t$. Our aim below is to derive an equation for the reduced density matrix $\rho_c \equiv \mathrm{Tr}_{A,I}(\mu_c)$ describing the cavity mode and the atomic external motion, where $\mathrm{Tr}_{A,I}$ is a trace over the atomic internal DOFs, by perturbation theory to Eq. (17) in terms of the small parameters $\varepsilon_{1,2}$. The desired equation has deterministic terms accurate to second order in the perturbation $\varepsilon_{1,2}$ and a stochastic term accurate to linear order in the perturbation $\varepsilon_{1,2}$, i.e.,

$$d\rho_c = O\left(\varepsilon_1^2, \varepsilon_2^2\right)dt + O(\varepsilon_1, \varepsilon_2)dW(t). \tag{A1}$$

To this end, in the following we first analyze the structure of Eq. (17) in the internal dark- and bright-state basis and then carry out the adiabatic elimination.

1. Stochastic master equation in the dark- and bright-state basis

In order to perform the adiabatic elimination, we express the SME (17) of the main text in terms of $\{|D\rangle, |\pm\rangle, |t\rangle\}$, i.e., the eigenstates of the atomic internal Hamiltonian $\hat{H}_{A,I}$, defined in Eqs. (18) and (19). In terms of them, we have

$$\begin{aligned}
|e\rangle &= \frac{1}{\sqrt{2}}(|+\rangle - |-\rangle), \\
|g\rangle &= \frac{1}{\sqrt{2}}\cos\alpha(z)(|+\rangle + |-\rangle) + \sin\alpha(z)\,|D\rangle, \\
|r\rangle &= \frac{1}{\sqrt{2}}\sin\alpha(z)(|+\rangle + |-\rangle) - \cos\alpha(z)\,|D\rangle,
\end{aligned} \tag{A2}$$

with the mixing angle $\alpha(z)$ defined in Eq. (20). Equation (A2) allows us to express each term of the SME (17) in the new basis.

The atomic spontaneous-emission terms (i.e., the last two lines) of Eq. (17) can be readily simplified in this new basis, under the condition $\Gamma_t, \Gamma_e \ll \Omega(z), |\Delta_t|, |\Omega(z)/2 \pm \Delta_t|$. This condition allows us to neglect the fast rotating terms in the spontaneous-emission channels under the rotating-wave approximation. As a result, Eq. (17) can be expressed as

$$\begin{aligned}
d\mu_c = &-\frac{i}{\hbar}[\hat{H}_{A,I} + \hat{H}_{A,E} + \hat{H}_C + \hat{H}_{AC}, \mu_c]dt \\
&+ \kappa\mathcal{D}[\hat{c}]\mu_c dt + \sqrt{\kappa}\mathcal{H}[\hat{c}e^{-i\phi}]\mu_c dW(t) \\
&+ \frac{\Gamma_t}{2}\sum_{j=\pm}\mathcal{G}_2^{rt}[\hat{\sigma}_{jt}]\mu_c dt \\
&+ \frac{\Gamma_e}{2}\sum_{j=\pm}\left(P_{ge}\mathcal{G}_2^{ge}[\hat{\sigma}_{Dj}] + P_{re}\mathcal{G}_1^{re}[\hat{\sigma}_{Dj}]\right)\mu_c dt \\
&+ \frac{\Gamma_e}{4}\sum_{j,l=\pm}\left(P_{ge}\mathcal{G}_1^{ge}[\hat{\sigma}_{jl}] + P_{re}\mathcal{G}_2^{re}[\hat{\sigma}_{jl}]\right)\mu_c dt \\
&- \frac{\Gamma_e P_a}{4}\sum_{j=\pm}\{\hat{\sigma}_{jj}, \mu_c\}dt + \Gamma_t\mathcal{G}_1^{rt}[\hat{\sigma}_{Dt}]\mu_c dt.
\end{aligned} \tag{A3}$$

Here, to simplify the notation we have defined

$$\begin{aligned}
\mathcal{G}_1^{jn}[\bullet] &\equiv \int du\, N_{jn}(u)\mathcal{D}[e^{-iku\hat{z}}\cos\alpha(\hat{z})\bullet], \\
\mathcal{G}_2^{jn}[\bullet] &\equiv \int du\, N_{jn}(u)\mathcal{D}[e^{-iku\hat{z}}\sin\alpha(\hat{z})\bullet],
\end{aligned} \tag{A4}$$

with $j = r, g$; $n = e, t$; and $\bullet$ representing a general operator. In Eq. (A3), the atomic spontaneous emissions are described by the last three lines, which occur only between the internal (dressed) eigenstates as a result of the rotating-wave approximation.

Next we consider the expression of the rest of the terms (i.e., the first two lines) of Eq. (A3) in the new basis. We note that these terms are diagonal in $\{D, \pm, t\}$ except $\hat{H}_{A,E}$ and $\hat{H}_{AC}$, which we now analyze. We first look at $\hat{H}_{A,E} = \hat{p}_z^2/2m + V(\hat{z})$. Due to the position dependence of the dark and bright states, the momentum operator $\hat{p}_z$ is nondiagonal in this basis and acquires an additional gauge potential. We can write it as

$$\hat{p}_z = \sum_{i,j\in\{D,\pm,t\}}\langle i|\hat{p}_z|j\rangle\hat{\sigma}_{ij} = -i\hbar\partial_z \otimes \mathbb{I} - \hat{A},$$

where the spatial derivative ∂_z acts only on the motional DOFs of the atom, $\mathbb{I} = \sum_{i\in\{D,\pm,t\}}|i\rangle\langle i|$ is the identity operator for the

internal states, and

$$\hat{A} = \left[\frac{i}{\sqrt{2}}\alpha'(\hat{\sigma}_{+D} + \hat{\sigma}_{-D}) + \text{H.c.}\right]$$

is a position-dependent vector potential which couples the internal dark state to the bright states. As a result, $\hat{H}_{A,E}$ is nondiagonal in the $\{D, \pm, t\}$ basis. Through straightforward calculation we find that it can be written as the sum of two parts $\hat{H}_{A,E} = \hat{H}^0_{A,E} + \hat{H}^1_{A,E}$. The first part does not couple the dark state to the bright states,

$$\hat{H}^0_{A,E} = \left[-\frac{\hbar^2\partial_z^2}{2m} + V(\hat{z})\right] \otimes \mathbb{I} + V_{\text{na}}(\hat{z}) \otimes \left(\hat{\sigma}_{DD} + \frac{1}{2}\sum_{i,j=\pm}\hat{\sigma}_{ij}\right). \tag{A5}$$

Here we have defined an effective potential for the atomic external motion

$$V_{\text{na}}(\hat{z}) \equiv \frac{\hbar^2}{2m}[\alpha'(\hat{z})]^2, \tag{A6}$$

which corresponds to the lowest-order nonadiabatic correction to the atomic external motion due to the spatially varying internal states. The second term $\hat{H}^1_{A,E}$ couples the dark state to the bright states,

$$\hat{H}^1_{A,E} = \frac{i\hbar}{2m}(\hat{A}\partial_z + \partial_z\hat{A}) = \hat{H}_1 \otimes (\hat{\sigma}_{+D} + \hat{\sigma}_{-D} + \text{H.c.}), \tag{A7}$$

with

$$\hat{H}_1 = -\frac{\hbar^2}{2\sqrt{2}m}(2\alpha'\partial_z + \alpha''). \tag{A8}$$

Similarly, the atom-cavity coupling Hamiltonian $\hat{H}_{AC} = \hbar g(\hat{z})(\hat{c}^\dagger\hat{\sigma}_{rt} + \text{H.c.})$ can be written as $\hat{H}_{AC} = \hat{H}^0_{AC} + \hat{H}^1_{AC}$; here

$$\hat{H}^0_{AC} = \frac{1}{\sqrt{2}}\hbar g(\hat{z})\sin\alpha(\hat{z})(\hat{c}\hat{\sigma}_{-t} + \hat{c}\hat{\sigma}_{+t} + \text{H.c.}) \tag{A9}$$

does not couple the dark state to the other states, while

$$\hat{H}^1_{AC} = \hbar\tilde{g}(\hat{z})\hat{c}\hat{\sigma}_{tD} + \text{H.c.} \tag{A10}$$

couples $|D\rangle$ to $|t\rangle$, with a strength

$$\tilde{g}(\hat{z}) \equiv -g(\hat{z})\cos\alpha(\hat{z}). \tag{A11}$$

In the following we will eliminate the atomic internal dynamics by perturbation theory in terms of the coupling Hamiltonians (A7) and (A10).

2. Adiabatic elimination

We now derive an effective equation of motion for the reduced density matrix $\rho_c \equiv \text{Tr}_{A,I}(\mu_c)$. To this end, we trace out the atomic internal DOFs on both sides of Eq. (A3), yielding

$$\begin{aligned} d\rho_c = {} & \mathcal{L}_0\rho_c dt + \sqrt{\kappa}\mathcal{H}[\hat{c}e^{-i\phi}]\rho_c dW(t) \\ & - \frac{i}{\hbar}[\hat{H}_1, \eta_+ + \eta_+^\dagger + \eta_- + \eta_-^\dagger]dt \\ & - i([\tilde{g}(\hat{z})\hat{c}^\dagger, \hat{\eta}_t] + [\tilde{g}(\hat{z})\hat{c}, \hat{\eta}_t^\dagger])dt + \frac{i}{\hbar}\Big[V_{\text{na}}(\hat{z}), \hat{\zeta}_t \\ & + \frac{1}{2}(\hat{\zeta}_+ + \hat{\zeta}_-)\Big]dt + \Gamma_t\big(\mathcal{K}_1^{rt} + \mathcal{K}_2^{rt} - 1\big)\hat{\zeta}_t dt \\ & + \frac{\Gamma_e}{2}\left[\sum_{j=g,r} P_{je}\big(\mathcal{K}_1^{je} + \mathcal{K}_2^{je}\big) - 1\right](\hat{\zeta}_+ + \hat{\zeta}_-)dt. \end{aligned} \tag{A12}$$

Here we have defined $\hat{\eta}_i \equiv \text{Tr}_{A,I}(\hat{\sigma}_{Di}\mu_c)$ and $\hat{\zeta}_i \equiv \text{Tr}_{A,I}(\hat{\sigma}_{ii}\mu_c)$, for $i \in \{t, \pm\}$, and have neglected terms proportional to $\text{Tr}_{A,I}(\hat{\sigma}_{\pm t}\mu_c)$ and to $\text{Tr}_{A,I}(\hat{\sigma}_{+-}\mu_c)$. In Eq. (A12) we have defined a superoperator

$$\mathcal{L}_0\rho_c = -\frac{i}{\hbar}\left[-\frac{\hbar^2\partial_z^2}{2m} + V(\hat{z}) + V_{\text{na}}(\hat{z}) + \hat{H}_C, \rho_c\right] + \kappa\mathcal{D}[\hat{c}]\rho_c \tag{A13}$$

which includes all the Hamiltonians in Eq. (A3) that do not couple the dark state to other internal states. We have also introduced the superoperators

$$\begin{aligned} \mathcal{K}_1^{jn}\bullet &\equiv \cos\alpha(\hat{z})\mathcal{K}^{jn}\bullet\cos\alpha(\hat{z}), \\ \mathcal{K}_2^{jn}\bullet &\equiv \sin\alpha(\hat{z})\mathcal{K}^{jn}\bullet\sin\alpha(\hat{z}), \end{aligned} \tag{A14}$$

where $\bullet$ stands for a general operator and the superoperator $\mathcal{K}^{jn}\bullet = \int du\, N_{jn}(u)e^{-ik_0u\hat{z}}\bullet e^{ik_0u\hat{z}}$ describes the momentum diffusion for the spontaneous-emission channel $|n\rangle \to |j\rangle$.

To solve for ρ_c in Eq. (A12), we should determine $\hat{\eta}_i$ and $\hat{\zeta}_i$. It is easy to see that $\hat{\eta}_i \sim O(\varepsilon_1, \varepsilon_2)$ and $\hat{\zeta}_i \sim O(\varepsilon_1^2, \varepsilon_2^2)$. Thus, to achieve the accuracy prescribed by Eq. (A1), we need to know the evolution of $\hat{\eta}_i$ accurate to a linear order deterministic term in $\varepsilon_{1,2}$ and to a constant stochastic term $d\hat{\eta}_i = O(\varepsilon_1, \varepsilon_2)dt + O(1)dW(t)$. They can be derived straightforwardly from Eq. (A3) as

$$\begin{aligned} d\hat{\eta}_\pm &= \frac{1}{2}\left[\mp i\Omega(\hat{z}) - \frac{\Gamma_e}{2}\right]\hat{\eta}_\pm dt + \mathcal{L}_0\hat{\eta}_\pm dt - \frac{i}{\hbar}\hat{H}_1\rho_c dt, \\ d\hat{\eta}_t &= \left(i\Delta_t - \frac{\Gamma_t}{2}\right)\hat{\eta}_t dt + \mathcal{L}_0\hat{\eta}_t dt - i\tilde{g}(\hat{z})\hat{c}\rho_c dt, \end{aligned} \tag{A15}$$

where on the RHS we have used the fact $\text{Tr}_{A,I}(\hat{\sigma}_{DD}\mu_c) = \rho_c + O(\varepsilon_1^2, \varepsilon_2^2)$. In Eq. (A15), stochastic terms drop out as they are of higher order, proportional to $O(\varepsilon_1, \varepsilon_2)$, than the desired accuracy. Moreover, under the adiabatic assumption, $\mathcal{L}_0$ can be neglected as it is far smaller than the atomic internal dynamics characterized by $\Omega(\hat{z})$, Δ_t, and $\Gamma_{e(t)}$. By keeping terms up to first order in $\Gamma_{e(t)}$ under the condition under the condition $\Gamma_t, \Gamma_e \ll \Omega(z), |\Delta_t|, |\Omega(z)/2 \pm \Delta_t|$, the above equations can be solved adiabatically to give

$$\begin{aligned} \hat{\eta}_\pm &= \frac{2}{\hbar}\Omega^{-2}(\hat{z})\left[\mp\Omega(\hat{z}) - i\frac{\Gamma_e}{2}\right]\hat{H}_1\rho_c, \\ \hat{\eta}_t &= \frac{1}{\Delta_t^2}\left(\Delta_t - i\frac{\Gamma_t}{2}\right)\tilde{g}(\hat{z})\hat{c}\rho_c. \end{aligned} \tag{A16}$$

Similarly, for $\hat{\zeta}_i$ we need to know their evolution accurate to second order in $\varepsilon_{1,2}$ for the deterministic terms and to linear

order in $\varepsilon_{1,2}$ for the stochastic term, $d\hat{\zeta}_i = O(\varepsilon_1^2, \varepsilon_2^2)dt + O(\varepsilon_1, \varepsilon_2)dW(t)$. They are given by

$$\begin{aligned} d\hat{\zeta}_t =& -\Gamma_t\hat{\zeta}_t + \mathcal{L}_0\hat{\zeta}_t dt - i[\tilde{g}(\hat{z})\hat{c}\hat{\eta}_t^\dagger - \hat{\eta}_t\tilde{g}(\hat{z})\hat{c}^\dagger]dt, \\ d\hat{\zeta}_\pm =& -\frac{\Gamma_e}{2}\hat{\zeta}_\pm dt + \mathcal{L}_0\hat{\zeta}_\pm dt - \frac{i}{\hbar}(\hat{H}_1\hat{\eta}_\pm^\dagger - \hat{\eta}_\pm\hat{H}_1)dt \\ &+ \frac{1}{2}\left[\Gamma_t\mathcal{K}_2^{rt}\hat{\zeta}_t + \frac{\Gamma_e}{2}\left(P_{ge}\mathcal{K}_1^{ge} + P_{re}\mathcal{K}_2^{re}\right)(\hat{\zeta}_+ + \hat{\zeta}_-)\right]dt. \end{aligned} \tag{A17}$$

The first equation can be solved adiabatically to give

$$\hat{\zeta}_t = \frac{1}{\Delta_t^2}\tilde{g}(\hat{z})\hat{c}\rho_c\tilde{g}(\hat{z})\hat{c}^\dagger. \tag{A18}$$

In solving the second equation, we make an expansion in the branching ratios $P_{ge}, P_{re} \ll 1$ and retain only first-order terms in P_{ge}, P_{re}. This will provide an effective evolution of ρ_c accurate to first order in P_{ge}, P_{re} [see the last line of Eq. (A12)]. We thus get

$$\begin{aligned} \hat{\zeta}_\pm =& \frac{\Gamma_t}{\Gamma_e}\left(1 + P_{ge}\mathcal{K}_1^{ge} + P_{re}\mathcal{K}_2^{re}\right)\mathcal{K}_2^{rt}\hat{\zeta}_t \\ &\pm \frac{4i}{\hbar^2\Gamma_e}[\hat{H}_1\rho_c\hat{H}_1\Omega^{-1}(\hat{z}) - \text{H.c.}] \\ &+ \frac{2}{\hbar^2}\left(1 + P_{ge}\mathcal{K}_1^{ge} + P_{re}\mathcal{K}_2^{re}\right)[\hat{H}_1\rho_c\hat{H}_1\Omega^{-2}(\hat{z}) + \text{H.c.}]. \end{aligned} \tag{A19}$$

Finally, we note that $\text{Tr}(\hat{c}\rho_c) = \text{Tr}(\hat{c}\mu_c) + O(\varepsilon_1^2, \varepsilon_2^2)$. Thus, with the accuracy prescribed by Eq. (A1), it is justified to express the quadrature in the nonlinear operator $\mathcal{H}[\hat{c}]$ in Eq. (A12) in terms of the reduced density matrix ρ_c, i.e., as $\langle\hat{c}\rangle_c = \text{Tr}(\hat{c}\rho_c)$.

Plugging these solutions into Eq. (A12), we find

$$\begin{aligned} d\rho_c =& \mathcal{L}_0\rho_c dt - \frac{i}{\hbar}[\hat{H}_{\text{coup}}, \rho_c]dt + \sqrt{\kappa}\mathcal{H}[\hat{c}e^{-i\phi}]\rho_c dW(t) \\ &+ \left(\frac{\Gamma_t}{\Delta_t^2}\mathcal{L}' + \mathcal{L}''\right)\rho_c dt. \end{aligned} \tag{A20}$$

Here $\mathcal{L}_0$ is defined in Eq. (A13), $\mathcal{H}[\hat{c}]\rho_c = (\hat{c} - \langle\hat{c}\rangle_c)\rho_c + \text{H.c.}$, with $\langle\hat{c}\rangle_c = \text{Tr}(\hat{c}\rho_c)$. Further,

$$\hat{H}_{\text{coup}} = \frac{\hbar g^2(\hat{z})}{\Delta_t}[\cos\alpha(\hat{z})]^2\hat{c}^\dagger\hat{c} \tag{A21}$$

is the desired local atom-cavity coupling. The Liouvillians $\mathcal{L}'$ and $\mathcal{L}''$ describes the effects of atomic spontaneous emission,

$$\begin{aligned} \mathcal{L}'\rho_c =& \left\{\mathcal{G}_1^{rt}[\tilde{g}(\hat{z})\hat{c}] + \mathcal{G}_2^{rt}[\tilde{g}(\hat{z})\hat{c}]\right\}\rho_c \\ &+ \left(P_{ge}\mathcal{K}_2^{ge} + P_{re}\mathcal{K}_1^{re} - 1\right)\mathcal{K}_2^{rt}[\tilde{g}(\hat{z})\hat{c}\rho_c\tilde{g}(\hat{z})\hat{c}^\dagger], \\ \mathcal{L}''\rho_c =& \frac{2\Gamma_e}{\hbar^2}\left(P_{ge}\mathcal{K}_2^{ge} + P_{re}\mathcal{K}_1^{re}\right)[\hat{H}_1\rho_c\hat{H}_1\Omega^{-2}(\hat{z}) + \text{H.c.}] \\ &- \frac{2}{\hbar^2}\Gamma_e\{\hat{H}_1\Omega^{-2}(\hat{z})\hat{H}_1, \rho_c\}. \end{aligned} \tag{A22}$$

We note that $\mathcal{L}''$ can be suppressed indefinitely small independently of $\hat{H}_{\text{coup}}$ by increasing the amplitude of Ω_g and $\Omega_r(z)$ while keeping their ratio fixed. In contrast, $\Gamma_t/\Delta_t^2\mathcal{L}'$ cannot be suppressed independently of $\hat{H}_{\text{coup}}$ and constitutes an essential imperfection to the operation of the microscope. We thus retain $\Gamma_t/\Delta_t^2\mathcal{L}'$ and neglect $\mathcal{L}''$ in the main text.

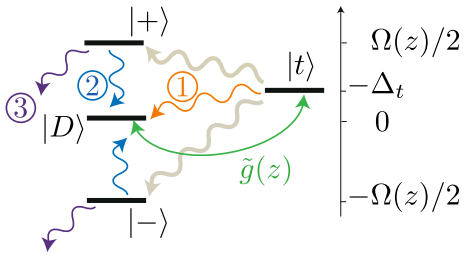

FIG. 11. Atomic dressed states and the spontaneous-emission channels relevant to Eq. (A23). The $|D\rangle \to |t\rangle$ transition interacts with the cavity mode with a strength $\tilde{g}(z) = -g(z)\cos\alpha(z)$, which leads to the local coupling (A21) in second-order perturbation theory. The wavy lines describe different spontaneous-emission channels; see the text for a detailed explanation.

Using Eqs. (A4) and (A14), we can write down the detailed form of $\mathcal{L}'$,

$$\begin{aligned} \mathcal{L}'\rho_c =& \int du\, N_{rt}(u)\mathcal{D}[\hat{c}e^{-ik_0u\hat{z}}\hat{v}_{z_0}]\rho_c \\ &+ P_{ge}\int du\, du'\, N_{rt}(u)N_{ge}(u') \\ &\times \mathcal{D}[\hat{c}e^{-ik_0(u+u')\hat{z}}\hat{w}_{z_0}\sin\hat{\alpha}_{z_0}]\rho_c \\ &+ P_{re}\int du\, du' N_{rt}(u)N_{re}(u') \\ &\times \mathcal{D}[\hat{c}e^{-ik_0(u+u')\hat{z}}\hat{v}_{z_0}\sin\hat{\alpha}_{z_0}]\rho_c \\ &- \frac{1}{2}\left\{\hat{c}^\dagger\hat{c}\left[\hat{w}_{z_0}^2\left(1 - P_{ge}\sin^2\hat{\alpha}_{z_0}\right) - P_{re}\hat{v}_{z_0}^2\sin^2\hat{\alpha}_{z_0}\right], \rho_c\right\} \end{aligned} \tag{A23}$$

Here we have used the shorthand notation $\hat{\alpha}_{z_0} \equiv \alpha(\hat{z})$ and have defined

$$\hat{v}_{z_0} = g(\hat{z})\cos^2\hat{\alpha}_{z_0}, \quad \hat{w}_{z_0} = g(\hat{z})\cos\hat{\alpha}_{z_0}\sin\hat{\alpha}_{z_0} = \hat{v}_{z_0}\tan\hat{\alpha}_{z_0}. \tag{A24}$$

The terms in Eq. (A23) are shown schematically in Fig. 11. Here the first line describes the process where the atom virtually absorbs a cavity photon and makes a transition from $|D\rangle$ to $|t\rangle$ and then decays back to $|D\rangle$ while spontaneously emitting a photon into free space, shown as channel 1 in Fig. 11. The second to fifth lines describe another possible route: After making a virtual transition from $|D\rangle$ to $|t\rangle$ by absorption of a cavity photon, the atom first spontaneously decays to the bright states $|\pm\rangle$ and then undergoes a second spontaneous emission to go back to $|D\rangle$, shown as channel 2 in Fig. 11. The last line is trace negative and describes the decay of the atomic population due to the spontaneous emission from $|\pm\rangle$ to states outside the four-level system, shown as channel 3 in Fig. 11.

Finally, the subwavelength condition $\sigma/\lambda_0 \ll 1$ (cf. Sec. III D) allows us to simplify Eq. (A23). Expanding Eq. (A23) in a power series of σ/λ_0, to the lowest order we can replace $\exp(-ik_0u\hat{z})$ by $\exp(-ik_0uz_0)$. Consequently, the momentum diffusion effect in the first three lines of Eq. (A23)

can be neglected and the mechanical effects on the atom are captured by the spatially localized operators $\hat{v}_{z_0}$, $\hat{w}_{z_0}$, and $\hat{\alpha}_{z_0}$. We will adopt this approximated expression for $\mathcal{L}'$ when deriving the spontaneous-emission-induced decoherence to the atomic external motion (C2).

APPENDIX B: CALCULATION OF THE SIGNAL-TO-NOISE RATIO

In this Appendix we detail the technique we adopt for calculating the SNR of the filtered homodyne current [cf. Eqs. (29) and (30)]. While the SNR can in principle be extracted, according to its definition (29) and (30), by statistical averaging over all measurement trajectories, this is practically inefficient. Instead, specific for the filter function (31), we can simplify the calculation by introducing an auxiliary cavity to the microscope setup as a physical filter. The SNR of the filtered homodyne current can thus be expressed in terms of the lower-order moments of the auxiliary cavity mode, which can be calculated straightforwardly by solving the corresponding cascade master equation.

Given the microscope setup (cf. Fig. 1), we consider feeding its output field to an auxiliary cavity mode. We denote the destruction (creation) operator of this auxiliary mode by $\hat{c}_{\rm a}$ ($\hat{c}_{\rm a}^\dagger$) and fix its frequency to be the same as the frequency of the microscope cavity. Moreover, we choose its linewidth as $\kappa_{\rm a}=2/\tau$, where τ is the filter integration time [cf. Eq. (31)]. From such a construction, the auxiliary cavity mode serves as a physical filter of the output field of the microscope. This is revealed most directly in the Heisenberg picture, in which the evolution of the auxiliary mode reads

$$\dot{\hat{c}}_{\rm a}(t)=-\frac{1}{\tau}\hat{c}_{\rm a}(t)-\sqrt{\frac{2}{\tau}}\hat{f}_{\rm out}(t), \tag{B1}$$

where $\hat{f}_{\rm out}(t)$ is the output field of the microscope. Equation (B1) can be integrated straightforwardly

$$\hat{c}_{\rm a}(t)=-\sqrt{\frac{2}{\tau}}\int_0^\infty dt' e^{-t'/\tau}\hat{f}_{\rm out}(t-t'). \tag{B2}$$

Comparing Eq. (B2) to Eqs. (29) and (31), we find that

$$\langle\mathcal{I}_\tau(t)\rangle_{\rm st}=-\langle\hat{X}_{\rm a}^\phi(t)\rangle/\sqrt{2\tau},\quad \langle\delta\mathcal{I}_\tau^2(t)\rangle_{\rm st}=\langle[\delta\hat{X}_{\rm a}^\phi(t)]^2\rangle/2\tau. \tag{B3}$$

Here we have defined the quadrature operator of the auxiliary cavity mode in the Heisenberg picture, $\hat{X}_{\rm a}^\phi(t)=e^{-i\phi}\hat{c}_{\rm a}(t)+e^{i\phi}\hat{c}_{\rm a}^\dagger(t)$, and its fluctuation $\delta\hat{X}_{\rm a}^\phi(t)=\hat{X}_{\rm a}^\phi(t)-\langle\hat{X}_{\rm a}^\phi(t)\rangle$, where $\langle\cdots\rangle\equiv{\rm Tr}[\varrho_0\cdots]$ is an expectation value with respect to the initial density matrix of the microscope plus the auxiliary cavity. Thus, the statistics (and thus the SNR) of the filtered homodyne current is directly imbedded in the lower-order moments of the auxiliary cavity mode.

In the above we adopt the Heisenberg picture to arrive at Eq. (B3). Nevertheless, to calculate Eq. (B3) it is more convenient to adopt the Schrödinger picture. In this picture, the RHS of Eq. (B3) can be expressed as $\langle\hat{X}_{\rm a}^\phi(t)\rangle={\rm Tr}[\hat{X}_{\rm a}^\phi\varrho(t)]$ and $\langle[\delta\hat{X}_{\rm a}^\phi(t)]^2\rangle={\rm Tr}[(\hat{X}_{\rm a}^\phi)^2\varrho(t)]-\{{\rm Tr}[\hat{X}_{\rm a}^\phi\varrho(t)]\}^2$, where $\hat{X}_{\rm a}^\phi=e^{-i\phi}\hat{c}_{\rm a}+e^{i\phi}\hat{c}_{\rm a}^\dagger$ and $\varrho(t)$ is the density matrix of the microscope plus the auxiliary cavity. It evolves according to the cascade master equation

$$\dot{\varrho}=-\frac{i}{\hbar}[\hat{H}_{A,E}+\hat{H}_C+\hat{H}_{\rm coup},\varrho]dt+\kappa\mathcal{D}[\hat{c}]\varrho dt+\frac{\Gamma_t}{\Delta_t^2}\mathcal{L}'\varrho dt$$
$$+\frac{2}{\tau}\mathcal{D}[\hat{c}_{\rm a}]\varrho-\sqrt{\frac{2\kappa}{\tau}}([\hat{c}_{\rm a}^\dagger,\hat{c}\varrho]+[\varrho\hat{c}^\dagger,\hat{c}_{\rm a}]). \tag{B4}$$

The first line of Eq. (B4) corresponds to the unconditional dynamics of the microscope setup [cf. Eq. (22)], with small terms proportional to $V_{\rm na}(\hat{z})$ and to $\mathcal{L}''$ neglected. The second line corresponds to the dynamics of the auxiliary cavity mode, which acts as a physical filter of the homodyne current. By numerically propagating Eq. (B4), we extract the statistics of the filtered homodyne current and thus the SNR.

APPENDIX C: PERTURBATIVE ELIMINATION OF THE CAVITY MODE

In this Appendix we derive the stochastic master equations (34) and (37) together with the corresponding homodyne currents (32) and (36), by eliminating the cavity mode perturbatively starting from Eqs. (22) and (23) of the joint atom-cavity system. This will allow us to relate the homodyne current to effective observables of the atom in the bad or good cavity limit and thus to define the two operation modes of the microscope.

We start by shifting away the stationary amplitude of the cavity field. Without coupling to the atom, the driven cavity mode populates a coherent state with amplitude $\alpha_0=-2\mathcal{E}/\sqrt{\kappa}$ (we assumed α_0 being real and $\alpha_0\gg1$ hereafter). We can shift it away via the transformations $\rho_c\to\hat{U}(\alpha_0)\rho_c\hat{U}(-\alpha_0)$, $\hat{H}\to\hat{U}(\alpha_0)\hat{H}\hat{U}(-\alpha_0)$, etc., with the unitary operator $\hat{U}(\alpha_0)=\exp(\alpha_0\hat{c}-\alpha_0\hat{c}^\dagger)$. As a result, Eq. (22) is transformed into

$$d\rho_c=-\frac{i}{\hbar}[\hat{H}_{A,E}+\hat{H}'_{\rm coup},\rho_c]dt+\kappa\mathcal{D}[\hat{c}]\rho_c dt$$
$$+\sqrt{\kappa}\mathcal{H}[\hat{c}e^{-i\phi}]\rho_c dW(t)+\frac{\gamma}{4\mathcal{C}}\mathcal{L}_{\rm sp}\rho_c dt. \tag{C1}$$

Here $\hat{H}'_{\rm coup}=\mathcal{A}f_{z_0}(\hat{z})(\hat{c}^\dagger\hat{c}+\alpha_0\hat{c}^\dagger+\alpha_0\hat{c})\simeq\alpha_0\mathcal{A}f_{z_0}(\hat{z})(\hat{c}^\dagger+\hat{c})$ and $\mathcal{L}_{\rm sp}$ is given by the replacement $\hat{c}\to\alpha_0$ in the expression of $\mathcal{L}'$ [see Eq. (A23)],

$$\mathcal{L}_{\rm sp}\rho=\mathcal{D}\big[f_{z_0}(\hat{z})\big]\rho+P_r\mathcal{D}\big[f_{z_0}(\hat{z})\sin\hat{\alpha}_{z_0}\big]\rho$$
$$+P_g\mathcal{D}\big[f_{z_0}(\hat{z})\tan\hat{\alpha}_{z_0}\sin\hat{\alpha}_{z_0}\big]\rho$$
$$-\tfrac{1}{2}\big\{f_{z_0}^2(\hat{z})\big[\tan^2\hat{\alpha}_{z_0}\big(1-P_g\sin^2\hat{\alpha}_{z_0}\big)$$
$$-P_r\sin^2\hat{\alpha}_{z_0}\big],\rho\big\}. \tag{C2}$$

In Eq. (C1) we have dropped an optical lattice potential $V_{\rm OL}(\hat{z})=\mathcal{A}f_{z_0}(\hat{z})\alpha_0^2$ due to the stationary cavity field, as it can be compensated straightforwardly by detuning the Raman resonance with a small offset $\Delta_r=g^2(z_0)\alpha_0^2/\Delta_t$. We have also neglected the small decoherence terms in $\mathcal{L}_{\rm sp}$ involving the fluctuations of the cavity field. Equation (23) is transformed to

$$I(t)dt=\sqrt{\kappa}\langle\hat{c}e^{-i\phi}+\hat{c}^\dagger e^{i\phi}\rangle_c dt+dW(t), \tag{C3}$$

where $\hat{c}$ and $\hat{c}^\dagger$ now correspond to the fluctuation of the cavity field and we have dropped a constant term contributed by the stationary cavity field.

Next we move to the interaction picture with respect to $\hat{H}_{A,E}$, the Hamiltonian for the atomic external motion. As a result, Eq. (C1) is transformed into

$$d\rho_c = -\frac{i}{\hbar}\mathcal{A}\alpha_0\big[\hat{f}_{z_0}(t)(\hat{c}+\hat{c}^\dagger),\rho_c\big]dt + \kappa\mathcal{D}[\hat{c}]\rho_c dt + \sqrt{\kappa}\mathcal{H}[\hat{c}e^{-i\phi}]\rho_c dW(t) + \frac{\gamma}{4\mathcal{C}}\mathcal{L}_{\rm sp}(t)\rho_c dt. \quad \text{(C4)}$$

Here we have defined in the interaction picture $\hat{f}_{z_0}(t) \equiv \exp(i\hat{H}_{A,E}t/\hbar)f_{z_0}(\hat{z})\exp(-i\hat{H}_{A,E}t/\hbar)$. We have also defined a time-dependent decoherence term $\mathcal{L}_{\rm sp}(t)$, of which the expression can be yielded by replacing $v_{z_0}(\hat{z})$ and $w_{z_0}(\hat{z})$ in Eq. (35) by the corresponding operators in the interaction picture. The expression for the homodyne current (C3) remains the same under this transformation.

Now we eliminate the cavity mode under the condition of weak atom-cavity coupling $\mathcal{A}\alpha_0 \ll \hbar\kappa$, by perturbation theory in the small parameter $\varepsilon = \mathcal{A}\alpha_0/\hbar\kappa$. We define a conditional density matrix for the atomic external motion $\tilde{\rho}_c \equiv {\rm Tr}_C(\rho_c)$, where ${\rm Tr}_C$ stands for tracing over the states of the cavity mode. Our aim is to derive an equation for the evolution of $\tilde{\rho}_c$ up to second order in the perturbation ε and up to a linear stochastic term

$$d\tilde{\rho}_c = O(\varepsilon^2)dt + O(\varepsilon)dW(t). \quad \text{(C5)}$$

To this end, we trace out the cavity DOF in Eq. (C4), yielding

$$d\tilde{\rho}_c = -\frac{i}{\hbar}\mathcal{A}\alpha_0\big[\hat{f}_{z_0}(t),\hat{\eta}+\hat{\eta}^\dagger\big]dt + \sqrt{\kappa}(\hat{\varsigma}e^{-i\phi}+{\rm H.c.})dW(t). \quad \text{(C6)}$$

Here $\hat{\eta} = {\rm Tr}_C(\hat{c}\rho_c)$ and $\hat{\varsigma} = \hat{\eta} - {\rm Tr}_S(\hat{\eta})\tilde{\rho}_c$, where ${\rm Tr}_S$ stands for tracing over the states of atomic external motion. The homodyne current can be related to $\hat{\eta}$ as

$$dq(t) \equiv I(t)dt = \sqrt{\kappa}[{\rm Tr}_S(\hat{\eta})e^{-i\phi} + {\rm c.c.}]dt + dW(t). \quad \text{(C7)}$$

To derive an equation for $\tilde{\rho}_c$ with the accuracy prescribed by Eq. (C5), we need to solve for $\hat{\eta}$ and $\hat{\varsigma}$ accurate to first order in the perturbation ε and up to a zeroth-order stochastic term. With this accuracy, their evolution is given by

$$d\hat{\eta} = -\frac{i}{\hbar}\mathcal{A}\alpha_0\hat{f}(t)\tilde{\rho}_c dt - \frac{\kappa}{2}\hat{\eta}dt,$$
$$d\hat{\varsigma} = -\frac{i}{\hbar}\mathcal{A}\alpha_0[\hat{f}(t) - \langle\hat{f}(t)\rangle_c]\tilde{\rho}_c dt - \frac{\kappa}{2}\hat{\varsigma}dt, \quad \text{(C8)}$$

where we have neglect terms involving $\mathcal{L}_{\rm sp}(t)$ in view of the smallness of the energy scale of $\mathcal{L}_{\rm sp}(t)$ compared to the cavity damping κ. By solving Eq. (C8) adiabatically and plugging these solutions back into Eq. (C6), we can derive an effective equation of motion for $\tilde{\rho}_c$. In the following we analyze the example of measuring a harmonically trapped atom and derive the effective equation of motion corresponding to the bad and good cavity limits separately.

1. Bad cavity limit

The bad cavity limit is defined by $\kappa \gg \omega$, i.e., the cavity dynamics is much faster than the atomic motion (quantified by its oscillation frequency ω) such that the former instantaneously follows the latter. Equation (C8) can thus be solved adiabatically

$$\hat{\eta} = -2i\alpha_0\frac{\mathcal{A}}{\hbar\kappa}\hat{f}(t)\tilde{\rho}_c, \quad \hat{\varsigma} = -2i\alpha_0\frac{\mathcal{A}}{\hbar\kappa}[\hat{f}(t) - \langle\hat{f}(t)\rangle_c]\tilde{\rho}_c. \quad \text{(C9)}$$

Plugging these solutions back into Eqs. (C6) and (C7), restoring the Schrödinger picture, and choosing the homodyne angle $\phi = -\pi/2$ to maximize the homodyne current, we arrive at Eqs. (34) and (32).

2. Good cavity limit

The good cavity limit is defined by $\kappa \ll \omega$, i.e., the cavity dynamics is much slower than the atomic motion. To solve Eq. (C8) in this limit, we expand the time-evolving focusing function in terms of its sidebands $\hat{f}_{z_0}(t) = \sum_\ell \hat{f}^{(\ell)}_{z_0}e^{-i\ell\omega t}$, with the ℓth sideband component $\hat{f}^{(\ell)}_{z_0} = \sum_n f_{n,n+\ell}|n\rangle\langle n+\ell|$ and $f_{mn} = \langle m|f_{z_0}(\hat{z})|n\rangle$. Assuming that $\tilde{\rho}_c$ depends on time slowly, Eq. (C8) can be integrated as

$$\hat{\eta} = -\frac{i}{\hbar}\mathcal{A}\alpha_0\sum_\ell\frac{\hat{f}^{(\ell)}_{z_0}e^{-i\ell\omega t}}{\kappa/2 - i\ell\omega}\tilde{\rho}_c,$$
$$\hat{\varsigma} = -\frac{i}{\hbar}\mathcal{A}\alpha_0\sum_\ell\frac{(\hat{f}^{(\ell)} - \langle\hat{f}^{(\ell)}\rangle_c)}{\kappa/2 - i\ell\omega}e^{-i\ell\omega t}\tilde{\rho}_c. \quad \text{(C10)}$$

Substituting these expressions into Eq. (C6), restoring the Schrödinger picture, and keeping only the nonrotating terms in the rotating-wave approximation, we obtain

$$d\tilde{\rho}_c = -\frac{i}{\hbar}[\hat{H}_{\rm eff},\tilde{\rho}_c]\,dt + \sum_\ell\frac{\gamma}{1+(2\omega\ell/\kappa)^2}\mathcal{D}\big[\hat{f}^{(\ell)}_{z_0}\big]\tilde{\rho}_c\,dt + \sqrt{\gamma}\sum_\ell\mathcal{H}\left[\frac{\hat{f}^{(\ell)}_{z_0}}{1-2i\ell\omega/\kappa}\right]\tilde{\rho}_c\,dW(t) + \frac{\gamma}{4\mathcal{C}}\mathcal{L}_{\rm sp}\tilde{\rho}_c dt, \quad \text{(C11)}$$

where

$$\hat{H}_{\rm eff} = \hat{H}_S + \sum_\ell\frac{\alpha_0^2\mathcal{A}^2\ell\omega/\hbar}{(\kappa/2)^2+\ell^2\omega^2}[\hat{f}^{(\ell)}\hat{f}^{(\ell)\dagger} - \hat{f}^{(\ell)\dagger}\hat{f}^{(\ell)}] \quad \text{(C12)}$$

and we have chosen the homodyne angle $\phi = -\pi/2$ to enhance the signal proportional to $\langle\hat{f}^{(0)}_{z_0}\rangle_c$. By filtering out higher sideband components corresponding to $\ell \neq 0$ in the homodyne current with a classical filter, the homodyne current can be expressed as

$$dq(t) \equiv I(t)dt = 2\sqrt{\gamma}\big\langle\hat{f}^{(0)}_{z_0}\big\rangle_c dt + dW(t), \quad \text{(C13)}$$

which recovers Eq. (36). Since these higher sideband components are not resolved, we can drop the stochastic terms with $\ell \neq 0$ in Eq. (C11), corresponding to averaging over these unobserved measurement channels. Finally, in the good cavity limit $\kappa \ll \omega$, the second term in the Hamiltonian $\hat{H}_{\rm eff}$ [cf. Eq. (C12)] is much smaller than $\hat{H}_S$ and can be neglected. We thus arrive at Eq. (37).

[1] D. Yang, C. Laflamme, D. V. Vasilyev, M. A. Baranov, and P. Zoller, Phys. Rev. Lett. **120**, 133601 (2018).

[2] For a review, see S. Kuhr, Natl. Sci. Rev. **3**, 170 (2016), and references therein.

[3] V. B. Braginsky and F. Y. Khalili, *Quantum Measurement* (Cambridge University Press, Cambridge, 1992).

[4] H. M. Wiseman and G. J. Milburn, *Quantum Measurement and Control* (Cambridge University Press, Cambridge, 2009).

[5] C. Gardiner and P. Zoller, *The Quantum World of Ultra-Cold Atoms and Light Book II* (ICP, London, 2015).

[6] H. Zhang, R. McConnell, S. Ćuk, Q. Lin, M. H. Schleier-Smith, I. D. Leroux, and V. Vuletić, Phys. Rev. Lett. **109**, 133603 (2012).

[7] S. Schreppler, N. Spethmann, N. Brahms, T. Botter, M. Barrios, and D. M. Stamper-Kurn, Science **344**, 1486 (2014).

[8] D. A. Steck, K. Jacobs, H. Mabuchi, T. Bhattacharya, and S. Habib, Phys. Rev. Lett. **92**, 223004 (2004).

[9] M. D. Lee and J. Ruostekoski, Phys. Rev. A **90**, 023628 (2014).

[10] A. C. J. Wade, J. F. Sherson, and K. Mølmer, Phys. Rev. Lett. **115**, 060401 (2015).

[11] G. Mazzucchi, S. F. Caballero-Benitez, D. A. Ivanov, and I. B. Mekhov, Optica **3**, 1213 (2016).

[12] Y. Ashida and M. Ueda, Phys. Rev. A **95**, 022124 (2017).

[13] C. Laflamme, D. Yang, and P. Zoller, Phys. Rev. A **95**, 043843 (2017).

[14] G. S. Agarwal and K. T. Kapale, J. Phys. B **39**, 3437 (2006).

[15] A. V. Gorshkov, L. Jiang, M. Greiner, P. Zoller, and M. D. Lukin, Phys. Rev. Lett. **100**, 093005 (2008).

[16] J. A. Miles, Z. J. Simmons, and D. D. Yavuz, Phys. Rev. X **3**, 031014 (2013).

[17] J. A. Miles, D. Das, Z. J. Simmons, and D. D. Yavuz, Phys. Rev. A **92**, 033838 (2015).

[18] K. D. Stokes, C. Schnurr, J. R. Gardner, M. Marable, G. R. Welch, and J. E. Thomas, Phys. Rev. Lett. **67**, 1997 (1991).

[19] C. Weitenberg, M. Endres, J. F. Sherson, M. Cheneau, P. Schausz, T. Fukuhara, I. Bloch, and S. Kuhr, Nature (London) **471**, 319 (2011).

[20] P. C. Maurer, J. R. Maze, P. L. Stanwix, L. Jiang, A. V. Gorshkov, A. A. Zibrov, B. Harke, J. S. Hodges, A. S. Zibrov, A. Yacoby, D. Twitchen, S. W. Hell, R. L. Walsworth, and M. D. Lukin, Nat. Phys. **6**, 912 (2010).

[21] Y. Ashida and M. Ueda, Phys. Rev. Lett. **115**, 095301 (2015).

[22] M. Łacki, M. A. Baranov, H. Pichler, and P. Zoller, Phys. Rev. Lett. **117**, 233001 (2016).

[23] F. Jendrzejewski, S. Eckel, T. G. Tiecke, G. Juzeliūnas, G. K. Campbell, L. Jiang, and A. V. Gorshkov, Phys. Rev. A **94**, 063422 (2016).

[24] S. Gleyzes, S. Kuhr, C. Guerlin, J. Bernu, S. Deleglise, U. Busk Hoff, M. Brune, J.-M. Raimond, and S. Haroche, Nature (London) **446**, 297 (2007).

[25] B. R. Johnson, M. D. Reed, A. A. Houck, D. I. Schuster, L. S. Bishop, E. Ginossar, J. M. Gambetta, L. DiCarlo, L. Frunzio, S. M. Girvin, and R. J. Schoelkopf, Nat. Phys. **6**, 663 (2010).

[26] J. Volz, R. Gehr, G. Dubois, J. Estève, and J. Reichel, Nature (London) **475**, 210 (2011).

[27] G. Barontini, L. Hohmann, F. Haas, J. Estève, and J. Reichel, Science **349**, 1317 (2015).

[28] C. B. Møller, R. A. Thomas, G. Vasilakis, E. Zeuthen, Y. Tsaturyan, M. Balabas, K. Jensen, A. Schliesser, K. Hammerer, and E. S. Polzik, Nature (London) **547**, 191 (2017).

[29] S. Uchino, M. Ueda, and J.-P. Brantut, arXiv:1802.04024.

[30] A. A. Clerk, M. H. Devoret, S. M. Girvin, F. Marquardt, and R. J. Schoelkopf, Rev. Mod. Phys. **82**, 1155 (2010).

[31] H. Ritsch, P. Domokos, F. Brennecke, and T. Esslinger, Rev. Mod. Phys. **85**, 553 (2013).

[32] T. E. Northup and R. Blatt, Nat. Photon. **8**, 356 (2014).

[33] H. Krauter, D. Salart, C. A. Muschik, J. M. Petersen, H. Shen, T. Fernholz, and E. S. Polzik, Nat. Phys. **9**, 400 (2013).

[34] Y. Wang, S. Subhankar, P. Bienias, M. Łacki, T.-C. Tsui, M. A. Baranov, A. V. Gorshkov, P. Zoller, J. V. Porto, and S. L. Rolston, Phys. Rev. Lett. **120**, 083601 (2018).

[35] B. Casabone, K. Friebe, B. Brandstätter, K. Schüppert, R. Blatt, and T. E. Northup, Phys. Rev. Lett. **114**, 023602 (2015).

[36] M. Wolke, J. Klinner, H. Keßler, and A. Hemmerich, Science **337**, 75 (2012).

[37] C. J. Hood, M. S. Chapman, T. W. Lynn, and H. J. Kimble, Phys. Rev. Lett. **80**, 4157 (1998).

[38] J. Johansson, P. Nation, and F. Nori, Comput. Phys. Commun. **184**, 1234 (2013).